# A rational hybrid RANS-LES model for CFD predictions of microclimate and environmental quality in real urban structures

Hadžiabdić, Muhamed; Hafizović, Mahir; Ničeno, Bojan; Hanjalić, Kemal

**DOI**
10.1016/j.buildenv.2022.109042

**Publication date**
2022

**Document Version**
Final published version

**Published in**
Building and Environment

Building and Environment 217 (2022) 109042

Contents lists available at ScienceDirect

Building and Environment

journal homepage: www.elsevier.com/locate/buildenv

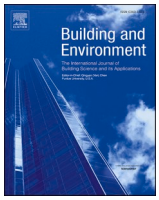

# A rational hybrid RANS-LES model for CFD predictions of microclimate and environmental quality in real urban structures

Muhamed Hadžiabdić [a,*], Mahir Hafizović [a,b], Bojan Ničeno [c], Kemal Hanjalić [d,e]

[a] International University of Sarajevo, Department of Engineering, Bosnia and Herzegovina
[b] Enova Consultants and Engineers, Podgaj 14, Sarajevo, Bosnia and Herzegovina
[c] Paul Scherrer Institute, Forschungsstrasse 111, 5232, Villigen, Switzerland
[d] Delft University of Technology, Mekelweg 5, 2628 CD, Delft, the Netherlands
[e] University of Sarajevo, Obala Kulina bana 7, Sarajevo, Bosnia and Herzegovina

ARTICLE INFO

*Keywords:*
Hybrid RANS-LES
URANS
Urban environment
Pollutant dispersion
Urban wind flow

ABSTRACT

We report on the application and comparative assessment of two rational turbulence modelling approaches for the computer simulation of air flow and pollutant dispersion in real urban environment: a stand-alone unsteady Reynolds-averaged Navier-Stokes eddy-viscosity model (URANS), and its blend with Large-eddy simulations (LES) in a hybrid mode (HRL). The elliptic-relaxation $(k-\varepsilon)\zeta-f$eddy-viscosity model was applied in both methods. The models, verified earlier in a range of engineering flows including heat transfer, were here validated in two environmental benchmark cases, a single building and an idealized urban settlement, both subjected to a steady wind. The velocity field and pollutant concentration are better predicted by the HRL method in both benchmarks. The HRL is then applied to predictions of air flow and spreading of pollutant from road traffic in downtown of a real city (Sarajevo) containing 100 realistic buildings. The simulations were performed with the in-house open-source CFD code T-Flows, specifically optimized for a fast and efficient high-quality unstructured meshing of the terrain orography and building configurations. The benchmark validations demonstrated that, compared with the standard $k-\varepsilon$, in typical urban applications with complex urban shapes and arrangements the accuracy and credibility of the predictions can substantially be improved by applying a physically sounder and yet still relatively simple $\zeta-f$ eddy-viscosity model that specifically accounts for the elliptic inviscid wall-blocking effects and near-wall stress anisotropy. The benchmarking also showed that still further improvements are achieved by using the HRL scheme which ensures a rational balance in capturing the important physics and the computational economy.

## 1. Introduction

Computational Fluid Dynamics (CFD) has emerged as a powerful method for researching, assessing and managing the impact of wind and pollution on outdoor and indoor climate and their effects on human comfort and health. Its potential has now been widely recognized by urban and land-use planners and designers as an indispensable decision-supporting tool for evaluating, predicting and optimizing the urban environmental quality parameters and their relations with urban topology for various meteorological and design conditions and scenarios.

However, despite the remarkable advances in CFD in general and its wide-spread use in just about all branches of engineering and applied science, a number of issues still pose challenges, especially for some specific applications including environmental flows, calling for further improvements of the simulation accuracy as well as the computational flexibility and economy. To this point we recall that in the essence of CFD are the fluid flow and related physical transport processes governed by complex physics and, in most cases, dominated by the dynamics of fluid turbulence, which impose specific requirements on the mathematical models of physical processes capable of returning trustful simulation results. Since such models unavoidably rely on approximate description ('modelling') of various physical phenomena and processes, the models as well as many other assumptions and simplifications, need to be validated and verified in a range of well-documented benchmark situations relevant for processes encountered in environmental physics before being employed for prediction purposes.

Over the last decade, a plethora of publications appeared dealing with CFD modelling processes in urban physics in general and in particular the air flow and pollutant dispersion. Several extensive

* Corresponding author. Hrasnička cesta 15, 71210, Ilidža, Bosnia and Herzegovina.
*E-mail address:* mhadziabdic@ius.edu.ba (M. Hadžiabdić).

https://doi.org/10.1016/j.buildenv.2022.109042
Received 30 January 2022; Received in revised form 24 March 2022; Accepted 26 March 2022
Available online 8 April 2022

**Nomenclature**

| | |
|---|---|
| $k$ | turbulent kinetic energy [$m^2/s^2$] |
| $\varepsilon$ | dissipation rate of turbulent kinetic energy [$m^2/s^3$] |
| $\zeta$ | non – dimensional velocity scale |
| $f$ | elliptic relaxation function |
| $U_i$ | velocity vector [m/s] |
| $H$ | Case 1: height of the building (0.16 m); Case 2: height of the small obstacles (0.03175 m) |
| $U_\infty$ | (Case 2) free stream velocity (0.38 m/s) |
| q | tracer gas flow rate. Case 1: $4.585 \times 10^{-7}$ $m^3/s$; Case 2: $2 \times 10^{-7}$ $m^3/s$ |
| $S_c''$ | (Case 3) line source intensity [$\mu g/m^3/s$] |
| $P$ | pressure [Pa] |
| $C$ | species concentration [$kg/m^3$] |
| $z_0$ | aerodynamic roughness length [m] |
| $z^+$ | non – dimensional wall distance |
| $x_i$ | space coordinates [m] |
| $U_H$ | (Case 1) inflow mean streamwise velocity component at the building height H (1.37 m/s) |
| $N_V$ | (Case 3) number of vehicles per hour [vehicles/hour] |
| $E_Q$ | (Case 3) mass of emitted particles per kilometre per vehicle (0.0216 g/km/vehicle) |
| $N_{lanes}$ | (Case 3) number of lanes for each street |

reviews discuss a spectrum of topics relevant to urban flows - the optimal solution domain and urban structure representation, computational grid generation and optimization, inflow and boundary conditions, numerical discretisation and solution and others (Tominaga and Stathopoulos [1], Di Sabatino et al. [2], Blocken [3], Blocken [4]). The performance of turbulence models has also been in focus of a number of papers, but in most cases the choice is limited to the rudimentary eddy viscosity schemes usually adopted from the menu offered by the available, usually commercial, CFD software codes. Interestingly, apart from few exceptions, in just about all CFD studies the computations have been conducted in 3D *steady* RANS mode.

Most popular benchmark cases are flows over a single building or a cluster of buildings of the same or similar regular shapes representing an idealized urban environment. Air flow around an isolated obstacle/building, investigated in a number of wind or water tunnel experiments, has been especially a popular test case because of its clear definition and easy numerical meshing, but also because of the availability of the reference experimental and/or numerical, mostly LES data. Despite its relatively simple geometry, the physics of these flows involve some of the most relevant, but computationally still challenging features, such as flow separation and recirculation, swirling, stagnation zones, vortex shedding, ground boundary layer recovery and others. The criteria for benchmarking focus, however, usually on the quality of reproduction of the global time-averaged mean-flow features as the computations are usually run in a steady mode, thus *per se* incapable of resolving any time dynamics of the particular phenomena (e.g Ramponi and Blocken [5]; Tominaga [6]; Liu and Niu [7]; Van Hooff et al. [8]). Others consider pollution dispersion (Blocken et al. [9]; Yoshie et al. [10]; Tominaga and Stathopoulos [11]), or the effect of different shapes of the building on the flow patterns (Tominaga et al. [12]; Tominaga and Blocken [13]; Van Druenen et al. [14]). The recent publication of Tominaga and Stathopoulos [11] investigated pollutant dispersion around isolated cubical buildings with a focus on effect of large-scale fluctuations, especially in the separation zone behind the building, on the concentration field by using steady and unsteady RANS. The authors found that the prediction accuracy of the concentration fields depends strongly on the location of the pollutant source with small differences in the results of steady and unsteady RANS confirming the limitations of the $k-\varepsilon$ and $k-\omega$ SST models in predicting flows around bluff bodies with strong three-dimensionality and inherent unsteadiness. A general observation was that both steady and unsteady RANS solutions underestimate the wind intensity in the wake region due to underestimation of the turbulent kinetic energy (Yoshie et al. [15], Tominaga et al. [16]).

Publications on air flow over an idealized city configuration represented by a regular or staggered array of obstacles, studied also both numerically and experimentally, focus usually on the dispersion of pollutants (Branford et al. [17]; Coceal et al. [18]; Fuka et al. [19]; Santos et al. [20]), urban ventilation (Cheung and Liu [21]; Castro et al. [22]; Tong et al. [23]), or the influence of objects arrangement on the flow patterns (Meinders and Hanjalić [24]; Coceal et al. [25]; Xie et al. [26]; Carpentieri and Robins [27]; Ramponi et al. [28]).

The CFD studies of air flows and transport processes in actual, real shapes and scales urban environment are more scarce in the literature compared with those dealing with simpler generic configurations, partially because of the need for larger computational efforts, but primarily because of a lack of the available experimental or numerical data for validation. However, recently there has been a notable increase in the number of published papers focusing on specific real urban configurations. This trend testifies of an increased interest for better understanding of the urban physics in real situations. In most cases the CFD is used to compute three-dimensional wind velocity and pollutant concentration fields, which in turn are employed for predicting, solving and managing various issues, mostly related to urban ventilation, pollution mitigation and human comfort. Specific novel topics include breathability of urban segments, pedestrian comfort (Blocken and Carmeliet [29]), heat island effects, and various aspects of pollution dispersion (Xie and Castro [30]; Gousseau et al. [31]; Blocken et al. [32]; Toparlar et al. [33]; Gao et al. [34]; Antoniou et al. [35]). The recent publication of Antoniou et al. [35], in which CFD results are validated against high-resolution field measurements, emphasizes the importance of explicit modelling of ground objects in as much details as possible, and accurate specifications of construction materials in computational domain for thermal field computations. The authors reported that the most important reasons for deviations between the measured and computational results are the missing effects of trees and green fields, the geometrical simplifications, the use of wall functions for near wall treatment and deficiency of the used RANS in predicting wind flow and turbulence levels in the wake region of buildings.

We report here on the results obtained by URANS and dynamically-interfaced hybrid RANS-LES approach, both employing the elliptic $k-\varepsilon-\zeta-f$ linear eddy viscosity model (Hanjalić et al. [36]), for two benchmark cases of idealized urban structures: a single building with a pollution source behind it, and a matrix of equally spaced cubical objects with a tall building in the middle, all subjected to a steady wind with a pollution source placed at the ground behind tower. The paper then focuses on the hybrid RANS-LES simulation of air flow and dispersion of traffic-generated pollutants carried out over a real-scale segment of the City of Sarajevo downtown with a realistic replica of about all important buildings and their shapes.

The computations were performed using the in–house unstructured finite-volume code T-Flows (https://github.com/DelNov/T-Flows), developed at TU Delft by Ničeno [37], Ničeno and Hanjalić [38]. T-Flows was extensively tested and validated over the years for LES (Hadžiabdić [39]), Delibra et al. [40], Borello et al. [41]); (U)RANS (Palkin et al. [42]; van Reeuwijk and Hadžiabdić [43]) and hybrid (Temmerman et al. [44]; Delibra et al. [40]) solution in the research of a variety of turbulent flows and transport processes.

## 2. Turbulence modelling for environmental flows: specificities and model choice

The first issue, when turbulence modelling is considered, is the choice between different modelling strategies, which can provide the optimum balance between capturing important physics and computa-

tional economy. The main feasible options currently available for CFD for environmental flows are the *steady* and *unsteady* Reynolds-averaged Navier-Stokes (SRANS, URANS), Large Eddy Simulation (LES), and their blend – a Hybrid RANS-LES (HRL). Undoubtedly, the true (properly resolved) LES is by far the most comprehensive and least empirical simulation method, but it is computationally too demanding and thus impractical for real-scale Reynolds and Rayleigh numbers flows, especially for complex terrain and urban topography (Yoshie et al. [15], Blocken [4]). On the other hand, the popular two–equation RANS models ($k-\varepsilon$ and $k-\omega$) and their revised ('improved') variants are known to fail in predicting accurately turbulent flows encountered in realistic urban settings in which, as noted above, fluid impingement, separation and other non-equilibrium turbulence interactions play a dominant role (Yoshie et al. [15], Tominaga et al. [16], Blocken et al. [9]). This is especially true when applying SRANS to complex urban configurations where three-dimensionality and intrinsic unsteadiness (e.g. vortex shedding) result in large-scale quasi-periodic fluid structures even when the wind is steady in the bulk. In such cases the URANS approach offers decisive advantage: treating and solving in time the governing equations as the *ensemble-averaged* should resolve the large-scale organised structures, and thus provide the associated *resolved* turbulent fluxes of momentum, heat and species in addition to the stochastic contributions provided by a turbulence model. However, it is noted that the choice of the model in the URANS mode also matters (Palkin et al. [45]).

As for the choice of the model, one can opt for higher-order RANS closures (non-linear eddy viscosity, second-moment transport models or their algebraic derivatives), but for complex configurations such methods may also prove to be computationally too demanding and inconvenient. We argue that a better and more practical option is a hybrid RANS-LES approach in which the RANS model is used in the near-wall/ground region and LES is applied elsewhere. However, although in the HRL approach the LES solutions fed across the RANS-LES interface into the RANS region may compensate for some shortcoming of the near-surface RANS model, the proper accounting for the near-wall physics and especially the inviscid blocking of the complex ground- and urban configuration, especially when the RANS region occupies a substantial portion of the flow, calls for a careful choice of the RANS scheme, preferably beyond the standard $k-\varepsilon$ and $k-\omega$ framework.

## 3. The adopted modelling rationale: elliptic-relaxation URANS and HRL

In the present study we adopted the elliptic relaxation $k-\varepsilon-\zeta-f$ (or for short, $\zeta-f$) eddy viscosity concept (Hanjalić et al. [36]) as the base model applied in URANS and hybrid RANS-LES (HRL) modes. The elliptic-relaxation approach (Durbin [46]) was developed specifically to handle complex wall-bounded flows without resorting to empirical wall adjustment functions. The approach seems thus well suited both for the stand-alone URANS and for HRL, especially for flows over complex geometric topology at high Re numbers where the RANS region may occupy more than just the attached portion of the flow.

The $\zeta-f$ model is a three-equation eddy viscosity model based on the conventional $k-\varepsilon$ concept, enhanced by the transport equation for $\zeta=v^2/k$, where $v^2$ is the Durbin's scalar surrogate for the wall-normal turbulent stress components. The equation set is complemented by a simple undemanding elliptic equation for the relaxation function $f$ with the original Durbin [46] time- and length-scale realizability limiters. The experience shows that the computational penalty for solving two additional equations (for $\zeta$ and $f$) is modest since the equations are simple and well coupled, ensuring fast convergence. Compared with the parent $v^2-f$ model of Durbin, the $\zeta-f$ requires less stiff wall boundary conditions and proved generally to be more robust and faster converging. The model main advantage over the popular linear eddy viscosity-based RANS models is a novel representation of the wall blocking effect through the elliptic relaxation. As the wall blocking effect is in its nature inviscid and non-local, the elliptic relaxation is more transparent and physically sounder approach than model modifications in terms of local flow properties as used in some revised versions of the common eddy-viscosity schemes. It also improves the predictions of momentum, heat and mass transfer in wall-bounded flows where turbulence anisotropy plays the crucial role.

Two features make the elliptic-relaxation approach particularly relevant for the application in urban configurations characterised by multiple versatile building morphology with decisive influence of the ground and walls on the turbulence structure and the flow as a whole. The first is the use of a scalar surrogate of the wall-normal stress ($v^2$) instead of $k$ as the near–wall turbulence velocity scale in the eddy-viscosity definition, which reflects directly the exact second-moment closure. In addition, the use of $v^2$ or $\zeta$ in the eddy-diffusivity for scalar flux diminishes the need for major adjustment of the turbulent Prandtl-Schmidt number from the common value of 0.9, a remedy followed in some studies to cure incorrect reproduction of the pollutant concentration field even if the mean velocity is well reproduced, e.g. Lateb et al. [47], Tominaga and Stathopoulos [48]. The second feature is the application of the elliptic relaxation concept to account for the inviscid wall blocking effect through the pressure reflection. Both features have a rational base as they stem from the more exact physical representation of the basic interaction in flows adjacent to solid surfaces.

The Navier-Stokes and the passive scalar transport equations in the RANS framework read:

$$\frac{\partial U_i}{\partial x_i}=0, \tag{1}$$

$$\frac{DU_i}{Dt}=-\frac{1}{\rho}\frac{\partial P}{\partial x_i}+\left(\nu\frac{\partial U_i}{\partial x_j}-\overline{u_iu_j}\right)+F_i \tag{2}$$

$$\frac{DC}{Dt}=\frac{\partial}{\partial x_j}\left(\frac{\nu}{\mathrm{Sc}}\frac{\partial C}{\partial x_j}-\overline{cu_j}\right)+S_c \tag{3}$$

in which $U_i$ is the velocity vector, $F_i$ is a body force per unit volume, $C$ denotes the species concentration per unit mass (considered as a passive scalar) and $S_c$ is the species source term per unit volume.

The momentum and species equations are closed by the linear eddy-viscosity/diffusivity models

$$\overline{u_iu_j}=-\nu_tS_{ij}+2k\delta_{ij}\Big/3, \qquad \overline{cu_j}=-\frac{\nu_t}{\mathrm{Sc}_t}\frac{\partial C}{\partial x_j} \tag{4}$$

where the turbulent Schmidt number is set to its standard value, $\mathrm{Sc}_t=0.9$.

The $\zeta-f$ model in its original form consists of the following equations, applied also in the ensemble-averaged framework:

$$\frac{Dk}{Dt}=\mathscr{D}_k+P_k-\varepsilon \tag{5}$$

$$\frac{D\varepsilon}{Dt}=\mathscr{D}_\varepsilon+\frac{c_{\varepsilon1}P_k-c_{\varepsilon2}\varepsilon}{\tau} \tag{6}$$

$$\frac{D\zeta}{Dt}=\mathscr{D}_\zeta+f-\frac{\zeta}{k}P_k \tag{7}$$

$$L^2\nabla^2f-f=\frac{1}{\tau}\left(c_1+c_2'\frac{P_k}{\varepsilon}\right)\left(\zeta-\frac{2}{3}\right) \tag{8}$$

$$\begin{aligned}\tau &= \max\left[\min\left(\frac{k}{\varepsilon},\frac{0.6}{\sqrt{6}\,c_\mu^v|S|\,\zeta}\right),\ c_\tau\left(\frac{\nu}{\varepsilon}\right)^{1/2}\right],\\ L &= C_L\max\left[\min\left(\frac{k^{3/2}}{\varepsilon},\frac{k^{1/2}}{\sqrt{6}\,c_\mu^v|S|\zeta}\right),\ c_\eta\left(\frac{\nu^3}{\varepsilon}\right)^{1/4}\right]\end{aligned} \tag{9}$$

$$\nu_t = c_\mu^v \zeta k \tau \tag{10}$$

where $k$ is the RANS ensemble modelled turbulent kinetic energy, $\varepsilon$ its dissipation rate, $P_k = \overline{u_i u_j}\frac{\partial U_i}{\partial x_j}$ is the production rate of turbulent kinetic energy, $\zeta = v^2/k$ is the velocity scale ratio, $f$ is an elliptic relaxation function and $\mathscr{D}$ denotes the total (molecular plus turbulent) diffusion

$$\mathscr{D}_\Phi = \frac{\partial}{\partial x_k}\left[\left(\frac{\nu}{\sigma_\Phi} + \frac{\nu_t}{\sigma_t}\right)\frac{\partial \Phi}{\partial x_k}\right] \tag{11}$$

The limiters, Eq (9), imposed on the turbulent time and length scales by Durbin [49], ensure the realizability constraints that include also the Kolmogorov time and length scales to account for viscosity effect for the grid points placed in the viscosity-affected wall layer – viscous sublayer and the buffer zone. However, in real urban environment characterised usually by very large Reynolds number, the computational mesh is usually too coarse to allow integration up to the walls (WIN approach), especially if the ground/wall surfaces are aerodynamically rough, so that the wall boundary conditions need to be treated by Wall Functions (WF). In such cases the viscous/molecular effects are uninfluential, and the Kolmogorov scales (as well as viscous/molecular diffusion terms) can be discarded so that only the first term (the true realizability limiters, 'min') in the square brackets of Eq. (9) remains active.

The hybrid version of the model, HRL model employs the $\zeta - f$ model only in the RANS region and the dynamic Smagorinsky model in the LES region. The rationale behind the HRL model (Hadžiabdić [39], Hanjalić [50], Hadžiabdić and Hanjalić [51]) is to intervene in the sink term of the $k$-equation with a grid-detecting parameter $\alpha$ (hence the approach sometimes also labelled as $\alpha$-HRL) by which the RANS eddy viscosity is suppressed to the subgrid-scale value of LES at the domains' matching interface. The model differs from the $\zeta - f$ model only in the $k$-equation with an addition of two limiters which control the switching from one to another model:

$$\frac{Dk}{Dt} = \mathscr{D}_k - P_k - \alpha\varepsilon \tag{12}$$

$$\alpha = max\left(1, \frac{L_{RANS}}{L_{LES}}\right),\ \nu_t = max\left(\nu_t^{RANS}, \nu_t^{LES}\right) \tag{13}$$

$$L_{RANS} = k^{1.5}\Big/\varepsilon \text{ and } L_{LES} = c_\Delta(\Delta V)^{1/3} \tag{14}$$

To function in a hybrid mode with LES in the outer flow region, the $k$-equation contains a blending function $\alpha$ associated with the energy dissipation rate $\varepsilon$, which, in the spirit of the DES practice, switches the implicit characteristic turbulence length scale from the RANS energy containing scale $L_{RANS}$ to the characteristic LES subgrid-scale when it becomes smaller than $L_{RANS}$. The model contains one more switching criterion which chooses the larger eddy viscosity among $\nu_t^{RANS}$ and $\nu_t^{LES}$. The model works in the URANS mode in the ground/wall-adjacent region where $\alpha = 1$. Away from solid surfaces, where $L_{RANS} > L_{LES}$, $\alpha > 1$, $k$ is damped, thus diminishing $\nu_t^{RANS}$. Eventually, when $\nu_t^{RANS} < \nu_t^{LES}$, the second constraint is activated, and the conventional LES is resumed. Depending on the active $\nu_t = \max(\nu_t^{LES}, \nu_t^{RANS})$, the model provides the RANS or the subgrid-scale (sgs) LES stress in the corresponding averaged or filtered momentum equations.

$$\tau_{ij} - \frac{1}{3}\tau_{kk}\delta_{ij} = -2\nu_t\overline{S_{ij}} \tag{15}$$

Where $\overline{S_{ij}}$ denotes the ensemble-RANS - or the filtered rate of strain tensor.

Once $\alpha$ becomes greater than 1, the RANS modelled eddy viscosity starts to decrease towards the LES sgs value, while the resolved energy increases. Thus, for $\alpha > 1$, the turbulence properties obtained from the $\zeta - f$ model do not represent any longer the characteristic large-eddy structures so that the length scale $L_{RANS}$ should be defined in terms of the total turbulent kinetic energy, $k_{tot} = k_{res} + k_{mod}$. In general, $k_{tot}$ is not known in advance, and the simulations can be started by using the mixing length $L_{RANS} = \kappa x_n$, where $x_n$ is the local distance from the nearest wall, until the flow structures are reasonably established, and then replaced by $L_{RANS} = k_{tot}^{1.5}/\varepsilon$. Using the standard $L_{RANS}$ throughout the model may sometimes pose some numerical instabilities in complex flow configurations which can be easily remedied by switching to $L_{RANS} = \kappa x_n$. It is noted, however, that, unlike in DES and similar schemes, here $L_{RANS}$ serves only to define the blending-control parameter $\alpha$, thus entering the turbulence model only in a narrow buffer region where $\alpha > 1$, which is usually only a few grid nodes between the true URANS ($\nu_t = \nu_t^{RANS}$) and the full LES ($\nu_t = \nu_t^{LES}$).

## 4. Ground/wall boundary conditions and terrain roughness modelling

In realistic urban configurations, air flow is characterised by high Reynolds number, with orders of magnitude typically reaching $10^6$ and higher. This inevitably implies the use of the Wall Functions (WF) for defining the boundary condition at walls since it is not feasible to have a mesh resolution sufficiently fine to resolve the boundary layer up to the wall as practiced in WIN (Wall Integration) schemes. The wall function approach is needed to estimate the wall shear stress as well as turbulent quantities in wall-adjacent cells. The roughness effect has also to be included as terrain is typically rough and not all objects on the ground can be explicitly modelled. The modification of the standard wall function that accounts for the surface roughness has been extensively discussed in the CFD community (e.g. Durbin et al. [52], Blocken et al. [53], Parente et al. [54], Toparlar et al. [55], among others). Two versions of the wall functions for the rough walls are the most used, the version based on the aerodynamic length $z_0$, and the $k_s$ – type wall function where the sand-grain roughness height $k_s$ is used. The $k_s$-based wall function's restrictive nature appears to be problematic especially for the urban configurations and Atmospheric Boundary Layer (ABL) computations (Blocken et al. [53]). Among the four requirements that need to be satisfied for the $k_s$-based wall function (details provided in Blocken et al. [53]), the one that asks for a cell-wall distance $z_P$ of the wall-adjacent cells to be larger than the physical roughness height $k_s$ ($k_s \approx 30z_0$) prove to be difficult to satisfy for the urban configurations where the roughness height $k_s$ is typically much larger than 1 m. This makes the $z_0$-based wall function a preferable choice for ABL computations as the restrictions present in the $k_s$ version do not apply.

The $z_0$-based wall function under a fully rough condition has the following form:

$$U^+ = \frac{U}{u_\tau} = \frac{1}{\kappa}\ln\left(\frac{z_P + z_0}{z_0}\right),\ z^+ = \frac{\rho u_\tau (z_P + z_0)}{\mu},\quad u_\tau = c_\mu^{1/4}k^{1/2} \tag{16}$$

$$\tau_{wall} = \frac{\kappa\rho c_\mu^{1/4}k^{1/2}U_P}{\ln(Ez_P^+)},\ P_k = \frac{\tau_{wall}c_\mu^{1/4}k^{1/2}}{\kappa(z_P + z_0)},\quad \varepsilon_P = \frac{u_\tau^3}{\kappa(z_P + z_0)} \tag{17}$$

$$\mu_{wall}^{eff} = \frac{\rho c_\mu^{1/4}k^{1/2}(z_P + z_0)}{U^+} \tag{18}$$

$$\theta^+ = Pr_t U^+ \tag{19}$$

We use $z_P$ to denote wall distance of the wall-adjacent cell centres as $z$ is the dominant wall-normal direction in the cases here considered. Obviously, the wall-normal direction is not limited to the $z$ direction as we are dealing with buildings walls and sloping terrain with hills and valleys. The aerodynamic roughness $z_0$ defines the $z$-origin where the mean velocity is zero, which, in the case of fully rough condition, does not coincide with the wall surface ($z = 0$) but it is shifted to $z = z_0$. We

defined $z_0$ in the computed cases by using the updated Davenport roughness classification of Wieringa [56].

It is worth emphasizing that the standard wall functions are based on the local turbulent kinetic energy equilibrium (production equals dissipation, no convection) which is hardly satisfied in complex three-dimensional and intrinsically unsteady flows typical for urban configurations. This shortcoming is partially overcome by obtaining the velocity and turbulent variables in the wall-adjacent cells by solving the full transport equations except for the turbulence dissipation which is imposed in the cell centre by the wall-function formulation. However, the wall function conditions are imposed in the momentum equation through the wall-shear stress $\tau_{wall}$ from which the velocity in the wall-nearest cell is evaluated from the classic log-law, and in the turbulent kinetic energy $k$ equation through its production term $P_k$ evaluated again in terms of $\tau_{wall}$. This means that the boundary conditions are still anchored to the semi-logarithmic velocity law and a fixed ratio of the local $k$ and $\tau_{wall}$ both valid strictly for wall-flows in local equilibrium. More general WF formulations accounting specifically for convection and pressure gradient have been proposed in the literature. A feasible option for urban fluid mechanics is the Generalised Wall Functions (Popovac and Hanjalić [57]) (labelled also Simplified Analytical Wall Functions (SAWF) in Hanjalić and Launder [58]) which proved to perform well in generic impinging and separating flows as well as in flows subjected to strong adverse and favourable pressure gradients. However, in view of the uncertainties involved in the definition of the characteristic roughness of the natural and built surfaces in the cases here considered, we leave this venture for some future studies.

## 5. Model validation

In order to assess and compare the performance of the two adopted approaches, the stand-alone URANS and its blend with LES in a hybrid mode, HRL, both using the elliptic-relaxation $\zeta - f$ model, we performed computations of the two benchmark cases with both approaches and the same boundary conditions and computational meshes. The CFD simulations were validated against the available experimental and some LES data. All variables are expressed in the SI base units.

### 5.1. Case 1: Flow and pollutant dispersion around a single building

#### 5.1.1. Computational details

A model of an isolated tall building, experimentally and numerically investigated by Yoshie et al. [10], was chosen for the numerical analysis of the air flow around a single building. Figure. 1(a) depicts the main characteristics of the case. The building's dimensions are $0.5H \times 0.5H \times H$, where $H$ is the height of the building. The building is placed in a turbulent air stream, with $\mathrm{Re} = \frac{U_H H}{\nu} = 15000$, based on the building height $H = 0.16$ m, and the mean velocity at the inflow at $H$ distance from the ground $U_H = 1.37$ m/s. As it can be seen in Fig. 1(a), a tracer gas (5% $C_2H_4$ ethylene, 30 °C) is injected through a circular opening in the ground, at the base behind the building, with a diameter of $0.03125H$. Yoshie et al. [10] performed the wind tunnel experiment in which the incoming air has a turbulent boundary layer generated by 26 thin aluminium ribs of a height of $0.05625H$ placed on the floor, perpendicular to the flow, as shown in Fig. 1(b). This generates a flow field that is difficult to reproduce without including the obstacles into the computational domain, which requires a very large number of cells. In addition to the experiments, Yoshie et al. [10] performed Large Eddy Simulation of the flow with two different inflow boundary conditions, without inflow turbulence (steady profiles imposed), and with the precursor domain with almost 10 million cells for that part alone. As the hybrid RANS-LES model requires three-dimensional, unsteady turbulent inflow, just like classical LES, the inflow condition is generated by using a precursor simulation with periodic boundary conditions in the stream- and spanwise directions with 15 obstacles (denoted in the text as precursor domain), see Fig. 1(d). Further in the text we denote this mesh as mesh A. The impact of the inflow condition on the URANS computation is less clear. In order to investigate it we performed the URANS

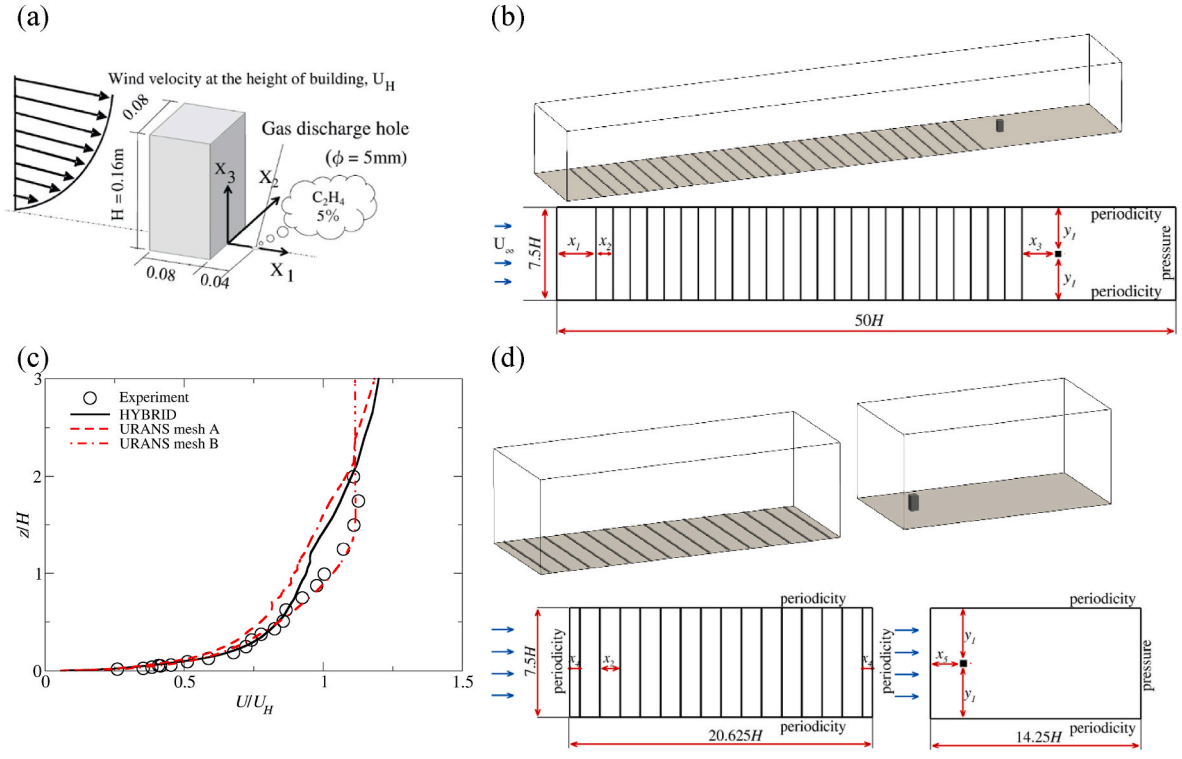


**Fig. 1.** (a) Sketch of the configuration used in the laboratory measurements. (Source: Yoshie et al. [10]), (b) Integral (mesh B) and (d) Precursor (mesh A) simulation domain with imposed boundary conditions. Characteristic distances: $x_1 = 3.125H$, $x_2 = 1.25H$, $x_3 = 2.625H$, $x_4 = 0.625H$, $x_5 = 2H$, $y_1 = 3.5H$, (c) Velocity profile at the inflow.

computations on two meshes, the mesh A with the precursor where the inflow for the main domain is generated by using the hybrid RANS-LES solution in the precursor, and mesh B, shown in Fig. 1(b), in which 26 ribs are placed in the same domain with the building. The fully developed flow is imposed at the inflow of the mesh B. The mesh A has around 15% less cells compared to the mesh B, but it results in a more realistic prediction of the turbulent field prior to the building. The velocity profiles at the centre of the domain and $2H$ upstream of the building obtained by the two mesh types and two models are shown in Fig. 1(c).

The mesh with the precursor, mesh A, has 1.49 million cells, out of which 970,000 cells are placed in the main domain while the precursor domain was meshed with approximately 520,000 cells. The precursor domain contains 165 $\times$ 40 uniformly distributed cells in stream- and spanwise directions, respectively. Double hyperbolic progression with 40 layers is used up to the building height, and 40 layers from the building's roof to the top. The centre of the first wall cell was located $4.0625 \times 10^{-3}H$ from the floor surface which results in maximum $z^+$ lower than 1. An open-source software Gmsh (Geuzaine and Remacle, [59]) is used to produce high quality unstructured mesh. The mesh B has around 1.7 million cells where the mesh resolution is very similar to the mesh A.

The no-slip condition was imposed at the bottom and top boundaries, as well as the building walls. The lateral sides were treated as periodic faces, and the pressure boundary condition was set at the outflow. The pollutant source was reconstructed as a square of area $766.6 \times 10^{-6}H^2$, with its centre located $0.25H$ from the back face of the building. It was treated as a separate inflow boundary condition with imposed gas flow rate of $q = 13.073 \times 10^{-6}U_H H^2$. The non-dimensional wall distance was kept below 5 for most of the domain for the URANS, and below 1 for the hybrid RANS-LES simulation. The case is treated as isothermal.

The SIMPLE algorithm is used for pressure-velocity coupling. The diffusion terms in all transport equations are discretised by using the second-order central difference scheme while the second-order TVD bounded convective scheme SMART of Gaskell and Lau [60] is applied to convective terms. The time integration is conducted by fully implicit second-order three-time-levels method. The non-dimensional time step is set to $\Delta t^* = \frac{tU_H}{H} = 0.0043$ for both URANS and hybrid RANS-LES, kept constant during the simulations, ensured the maximum CFL number around 1 for all computations.

Finally, the issue of economy of each method is addressed. This is an important issue since a typical computation of flow and pollutant transport in an urban environment requires a large computational grid with millions of computational cells. The current simulation was conducted on a modern workstation (Dell) on 36 processors (Intel Xeon Gold 6148 2.4 GHz) with 64 GB of available RAM memory. The total computational cost was around 3400 CPU hours (4 days) for HRL and 2160 CPU hours (2.5 days) for the URANS computation. The HRL method is some 35% more expensive, mainly due to a larger number of iterations for the pressure equation and longer computation time needed for collecting statistics as HRL resolves a broader spectrum of turbulent scales. Obviously, the higher accuracy and more reliable results do not come without a price.

#### 5.1.2. Results

We present the results obtained by two different modelling strategies, URANS with the $\zeta - f$ model, and hybrid RANS-LES model that combines the $\zeta - f$ and the dynamic Smagorinsky model. The URANS computations have been performed on both mesh A and mesh B with an aim to test the impact of the inflow condition on the URANS performance. It is important to note that the solution on the mesh B contains most of the turbulence energy modelled in front of the building, while the mesh A provides LES-like inflow where most of the turbulence field is resolved. As the HRL model produced similar results on both meshes, only the results obtained on the mesh A are presented.

Figure 2 shows the comparison of the mean flow features obtained by the URANS and HRL model. The mean statistics were collected over 10 "through flow" time units, after having reached a satisfactory developed flow. Although, the main characteristics of the flow are similar, some important differences can be discerned. The size of the horseshoe vortex in the URANS solution is larger, as well as the separation bubble formed in the wake of the building. The separation zones at the side walls and at the top of the building are predicted by both models but their sizes and positions differ.

How well these features compare to the measurements, can be seen in Fig. 3. In the left column, the measured and computed streamwise velocity fields are compared in the vertical mid-plane across the building. The main flow characteristics are well predicted by the HRL model, Fig. 3(c). The separated zone is somewhat overpredicted but with a shape similar to the measurements. The separations on the top and the bottom at the windward side of the building are well predicted as well. The two URANS solutions obtained on two different meshes significantly differ, especially in the wake region. The velocity field obtained on the mesh A is much closer to the measurements and similar to the hybrid RANS-LES solution. However, the solution obtained on the mesh B significantly overestimates the size of the separation bubble, see Fig. 4 (b), as well as the separation zone on the building's top. The overprediction of the wake region by the computational results is clearly visible in Fig. 4. It is interesting to note that the well-resolved LES performed by Yoshie et al. [10] also overpredicts the separation bubble compared to the experiments which indicates that ambiguity of the inflow condition is partly responsible for the differences that appear between the experimental and computational results. HRL and URANS on the mesh A are producing the wake which is slightly larger than the LES result. It seems that the unsteadiness imposed by the inflow generated in the precursor domain in the mesh A, helps to capture some dominant flow dynamics unlike in the integral domain (the mesh B), where the most of turbulence energy is modelled and only very large scales are resolved.

The concentration fields, shown in the right column of Fig. 3, follow the pattern of the predicted velocity fields. The general trend is that the pollutant in the computational results is more dispersed compared to the experiments. Like for the velocity field, HRL and URANS on the mesh A produce similar results, much closer to the experiments than the field

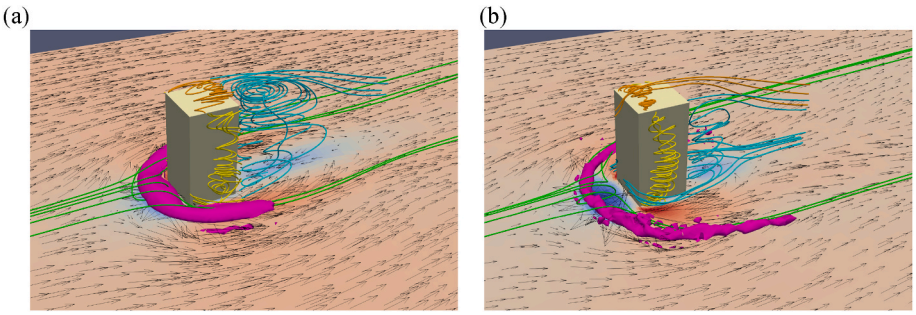


**Fig. 2.** Mean velocity field with corresponding streamlines and visualization of instantaneous horseshoe vortex (a) URANS result, (b) HRL result.

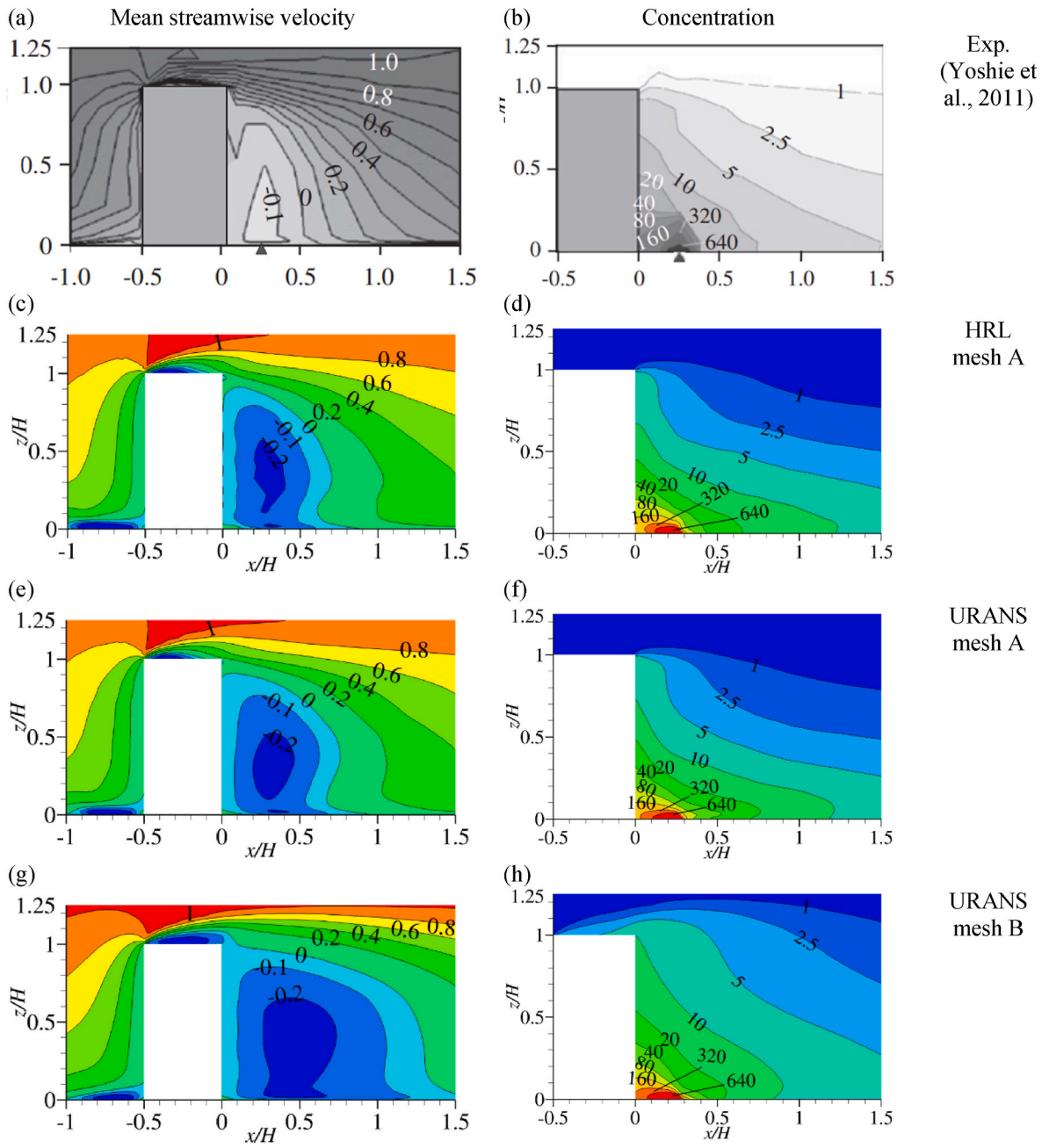


**Fig. 3.** Contours of normalized mean streamwise velocity $U/U_H$ (left) and the normalized concentration field $C{\cdot}U_H H^2/q$ (right) in the center plane.

obtained by URANS on the mesh B.

The differences in the wake predictions are reflected in the more quantitative comparisons of the velocity profiles. Figure 5 shows vertical profiles of the streamwise velocity behind the building in the center plane at four different locations, close to the building (0.125$H$) and further downstream (up to 1.5$H$). Close to the building leeward side, almost all profiles collapse into one line, Fig. 5(a), indicating pressure-gradient dominated region. However, further downstream the URANS on the mesh B produces a large discrepancy with the experimental data reflecting the overestimation of the separation zone. The URANS on the mesh A is much closer to the experiments and not much different from the HRL solution. It is interesting that the URANS results on the mesh B at $x/H = 0.625$ are similar to the LES results of Yoshie et al. [10] in which a uniform, steady inflow is imposed. Yoshie et al. [10] performed two LES computations, one with the precursor that mimics the experimental conditions and another with a uniform, steady velocity field at the inflow. The common feature of these two solutions at $x/H = 0.625$ is the underestimated level of turbulence.

The link between the turbulent stress field and the wake length can be better understood by looking into the simplified equation of the long-time averaged streamwise momentum along the centerline in the wake that reads

$$\frac{1}{\rho}\frac{\partial P}{\partial x} = -U\frac{\partial U}{\partial x} - \frac{\partial \overline{uu}}{\partial x} - \frac{\partial \overline{uv}}{\partial y} - \frac{\partial \overline{uw}}{\partial z} \tag{20}$$

where $u$, $v$, $w$ denote fluctuating velocity component in $x$, $y$, and $z$ directions.

A positive pressure gradient is balanced by convection and turbulent diffusion terms. If the turbulent diffusion transport is underpredicted, the convection term must increase to compensate it. As $\partial U/\partial x > 0$ for the second half of the wake region, the convection term $-U\partial U/\partial x$ can increase only if $U$ becomes negative, making the whole term positive.

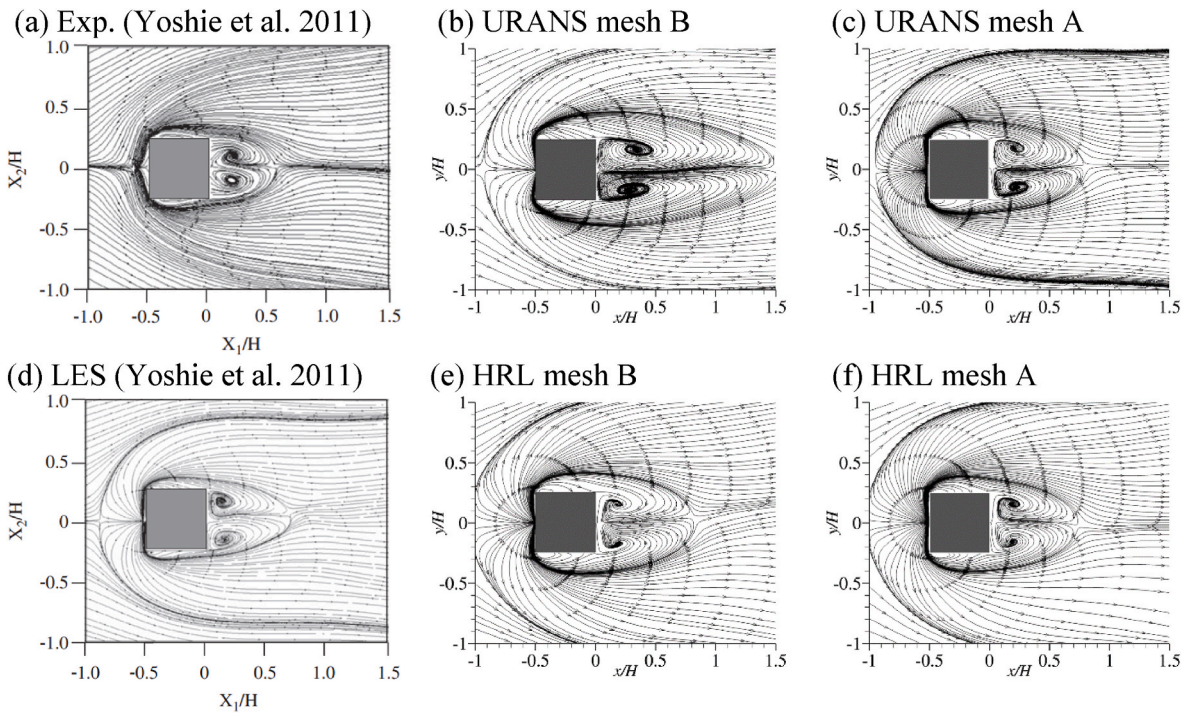


**Fig. 4.** Time-averaged streamlines of streamwise velocity $U$ in horizontal plane at $z = 0.025H$.

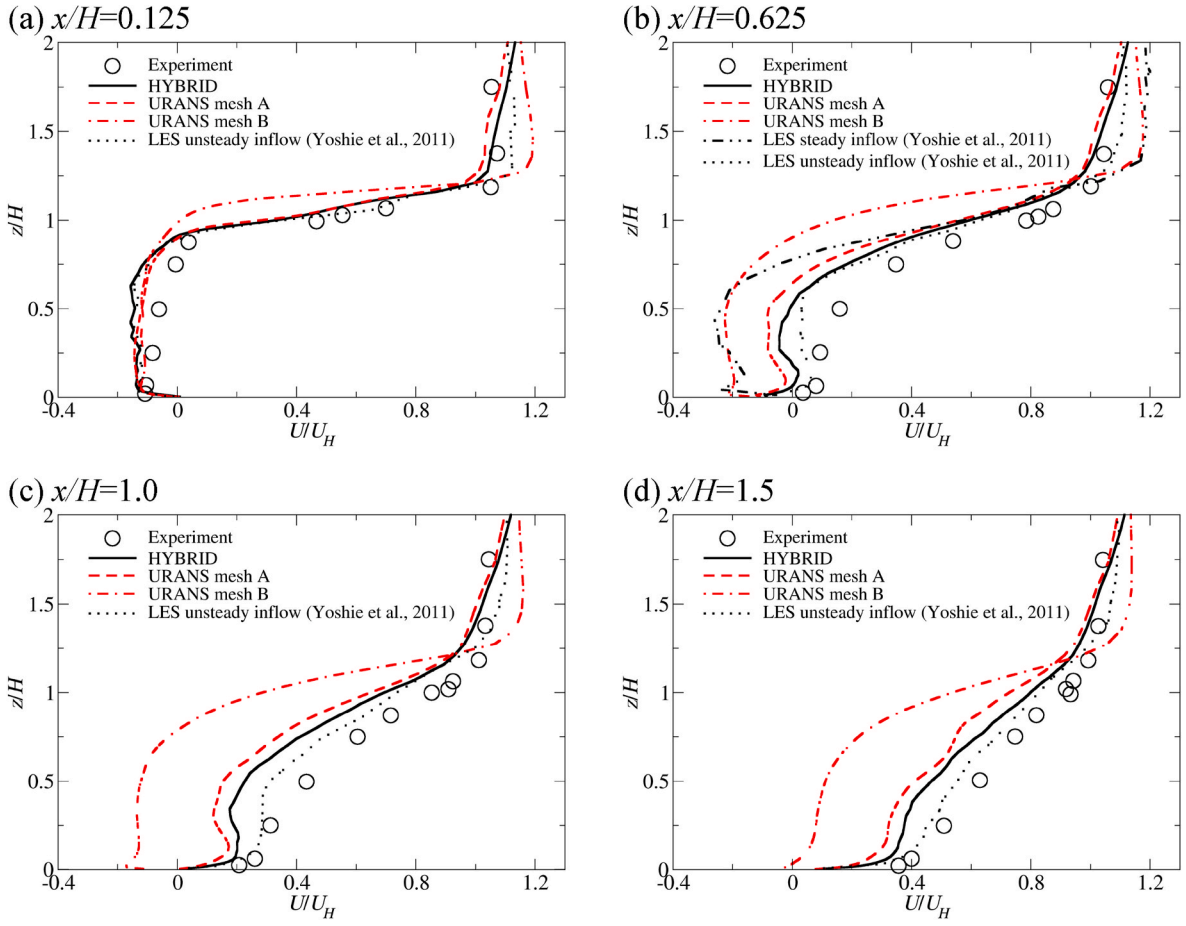


**Fig. 5.** Vertical profiles of streamwise velocity behind the building in center plane at several locations, (a) $x/H = 0.125$, (b) $x/H = 0.625$, (c) $x/H = 1.0$, (d) $x/H = 1.5$. The URANS results are shown for the integral mesh, B (denoted as 'mesh B'), and the precursor mesh, A (denoted as 'mesh A').

This means that underprediction of the turbulent stress field in the wake will lead to longer recirculation zone as the region of negative streamwise velocity has to increase. The turbulent diffusion term $\partial\overline{u_i u_j}/\partial x_j$ is modelled by the eddy viscosity within the URANS framework (with insufficient contribution of the resolved part), while it is mainly resolved in the HRL model as the sgs contribution is small.

As in the most flows over bluff bodies, unsteady quasi-periodic vortex shedding is forming the Kármán vortex street in the separating shear layers around the building. As a result, the convective transport is significant as the vortices produced by shedding are efficiently transporting momentum and turbulent kinetic energy from the periphery of the wake towards its center. These vortices play a significant role in penetrating the wake region and transporting the momentum and turbulence from the wake periphery to its center. The coherent structures are just partly resolved in the URANS solution on the mesh B as the flow is stabilized by a high level of the modelled turbulent stress and energy generated in the shear layer. This is clearly visible in the instantaneous streamlines plotted over the pressure field shown in Fig. 6(a), (b). The URANS solution on the mesh B resolves the two main large vortices in the wake while the hybrid solution contains a large number of smaller-scale structures generated in the wake shear layer. The differences in the convective transport of the turbulent kinetic energy by URANS and HRL can be seen in Fig. 6(c), (d) where the convective transport is estimated as $\overline{U_j}\partial\overline{k_{tot}}/\partial x_j$ where overbar denotes long-time averaging. This is not the exact convection as the statistical averaging of the $\overline{U_j\partial k_{tot}/\partial x_j}$ terms are needed for the exact convection. The convective transport of the turbulent kinetic energy in the wake is significantly smaller for the URANS on the mesh B. These results emphasize the importance of resolving the quasi-periodic vortex shedding events that dominate flow dynamics since the vortices generated in the process play the key role in momentum and mass transport.

### 5.2. Case 2: Flow and pollutant dispersion in idealized city with buildings and a single tower

#### 5.2.1. Computational details

The second benchmark case is air flow over an idealized urban settlement represented by a matrix of inline arranged objects on the ground

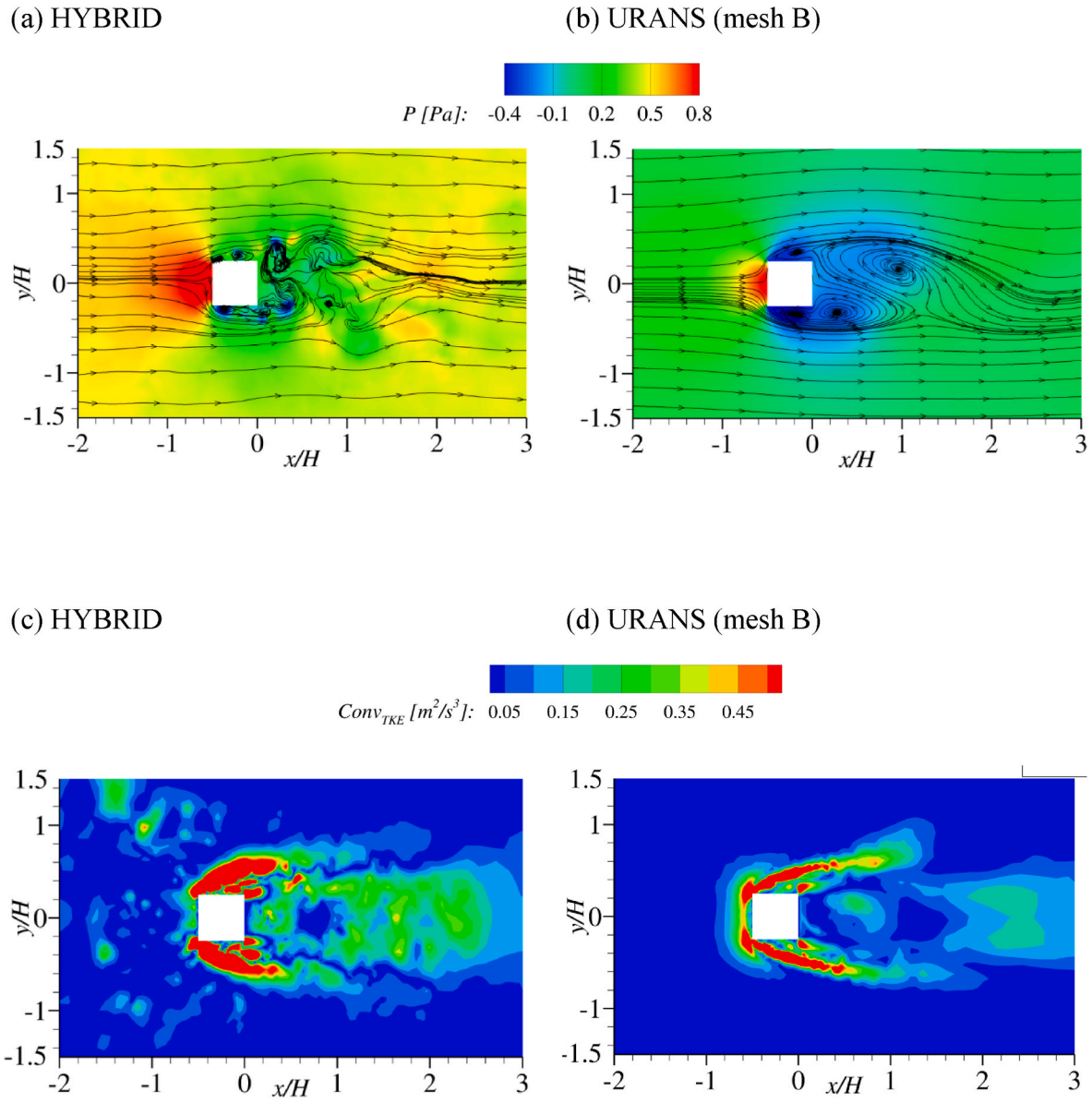


**Fig. 6.** (a) HRL and (b) URANS instantaneous pressure field with streamlines of the instantaneous velocity in the horizontal plane at $z = 0.5H$; (c) HRL and (d) URANS estimation of convective transport of turbulent kinetic energy at $z = 0.5H$ by $\overline{U_j}\partial\overline{k_{tot}}/\partial x_j$.

that was experimentally investigated by Hilderman and Chong [61]. The computational domain, shown in Fig. 7, mimics an urban segment with a matrix of orderly and equally spaced cubes of size $H$ and with a single tower of $3H$ height located in the centre of the domain. To economise the computational cost, the number of object columns has been reduced to 7 in the spanwise direction, while the number of rows remained the same. The distance between the obstacles on the ground is $H$. The pollutant source is placed in the middle of the canyon at the leeward side of the tower at the ground level. The pollutant enters the domain through a small vertical jet with an internal diameter of $0.0882H$ and a flow rate of $5.22 \times 10^{-4} U_\infty H^2$. The pollutant (dye tracer) has diffusivity of $5.2 \times 10^{-10}$ m$^2$/s. The Reynolds number of the flow is 36000 based on the tower height ($3H$) and the free flow velocity $U_\infty$, where we adopted $H = 0.03175$ m, $U_\infty = 0.38$ m/s.

The vertical domain dimension is discretised by 80 computational cells, where 65 cells were used up to the height of $3.2H$. The cells in this layer are hyperbolically clustered towards its ends (bottom and top of the tower). The nondimensional wall distance $z^+$ varies between 40 (in most of the domain) and 1 or less (in front of the tower). Here, the compound wall treatment proposed by Popovac and Hanjalić [57] is used to deal with the boundary conditons that smootlhy switches from the wall-integration (WIN) to the wall function (WF) boundary conditions. The computational mesh consists of 5 million cells. The pollution source was defined as an additional passive scalar flow input with an area and flow rate taken to be the same as in the experiments (a uniform vertical velocity of $0.0855U_\infty$).

The zero-gradient condition is imposed at the top and lateral boundaries, while the pressure boundary condition is applied at the outflow. No-slip condition for smooth walls is applied at the building walls, while at the ground the same characteristic aerodynamic roughness height is imposed as reported in the experiments. To ensure the undisturbed development of the flow, the boundaries are located at the distance from the obstacles in accordance with the recommendations (Franke et al. [62]). A fully developed flow generated by a separate simulation of the infinitely long channel flow is imposed at the inlet boundary for both the URANS and HRL computations. The presence of the obstacles before the pollutant source mitigates the influence of inflow conditions on the results by mixing the flow and thus making it less sensitive to the inflow conditions.

The same numerics are used as in the previous case. The nondimensional time step is set to $\Delta t^* = \frac{tU_\infty}{H} = 0.012$ for HRL and $\Delta t^* = 0.018$ for URANS, with the maximum CFL number around 1 for all computations.

### 5.2.2. Results

The mean streamwise velocity field and the corresponding turbulent kinetic energy are shown in Fig. 8. The statistics were collected over 8 "through flow" time units, after having reached a satisfactory developed flow. The main differences are visible in the shape and size of the recirculation zones behind the buildings and the tower. The HRL model produces smaller separation bubbles in the wakes of both types of objects compared to the URANS solutions. The separation bubble on the top of the first building after the tower is present in the URANS results while it does not appear in the HRL results. The separation bubbles formed on the side walls of the tower also differ in their location and size, being somewhat smaller and placed closer to the ground in the case of the URANS.

As in the single-building configuration, the URANS predicts a lower level of the turbulent kinetic energy, Fig. 8(g) and (h). This is especially the case in the wake of the tower but also in the wakes of the buildings. The turbulent kinetic energy penetration into the street canyons formed by small obstacles is more efficient in the HRL than in the URANS. More quantitative comparisons are given in Fig. 9 where vertical distribution of the mean streamwise velocity and turbulent kinetic energy at several locations are compared with the experiments. The velocity profiles from two models at the locations close to the tower, on the windward and leeward sides, follow the measured velocity and do not differ much even though the corresponding values of the turbulent kinetic energy are very different. This implies that the region close to the tower is pressure dominated and the velocity is not much influenced by turbulence. However, further downstream discrepancy in the velocity profiles is significant. As HRL predicts correct size of the separation region behind the tower, the velocity profile closely follows the experimental data while the URANS shows large differences in the velocity values.

Figure 9(a) shows profiles of the turbulent kinetic energy along a vertical line, $0.5H$ before the tower. The URANS solution severely underestimates the turbulent kinetic energy in the region up to the small obstacle's roof ($1H$), however it is slowly recovering as it reaches the tower height. The similar pattern repeats further downstream at locations $0.5H$ and $1.5H$ after the tower as shown in Fig. 9(b) and (c). The HRL results show good agreement with the experiment, both in the values and shape of the profiles, while the URANS underestimates the turbulent kinetic energy below the $3H$ line. As it was concluded in the single building case, the insufficient penetration of turbulence into the wake region, and in the street canyons, is the main reason for the poor prediction of the turbulence level. This leads to the overprediction of the bubble size. This is especially visible in Fig. 9(c) (left), which shows the mean streamwise velocity profiles along a vertical line in the wake of the tower. The URANS solution shows peaks of negative velocity in the region where HRL gives entirely positive values.

In Fig. 10 the concentration values are compared with the experiments at four locations, $1H$ in front of the source at the height of $3.25H$, exactly at the source at the height of $0.5H$, and $2H$ and $4H$ behind the source at heights $z = 3.25H$ and $z = 1.25H$respectively. The concentration profiles above the tower at $z = 3.25H$ show significant difference between the URANS and hybrid RANS-LES results, where the hybrid model is closer to the experiments. As the flow at the tower's top is characterized by a separation bubble that forms at the leading edge of the roof, even small differences in the predicted flow features can lead to large differences in the concentration values which are very low at this location far from the source. Further downstream at $x = 2H$ and the same height, both models predict the concentration level very well. Close to the surface, at $z = 0.5H$, the hybrid model predicts the concentration remarkable well at both locations, $x = 2H$and $x = 4H$. The

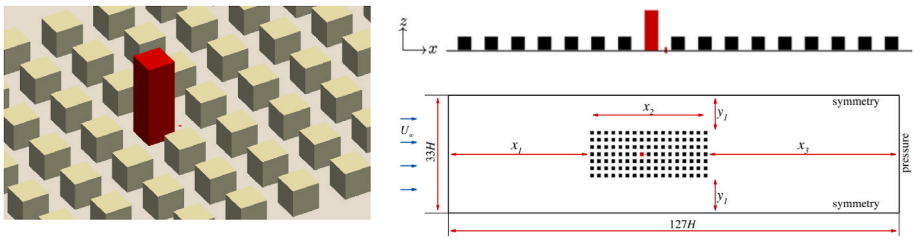


**Fig. 7.** Computational domain with imposed boundary conditions. The tower is colored in red, and the pollution source is represented by the red rectangle. Characteristic distances: $x_1 = 40H$, $x_2 = 33H$, $x_3 = 54H$, $y_1 = 10H$. (For interpretation of the references to color in this figure legend, the reader is referred to the Web version of this article.)

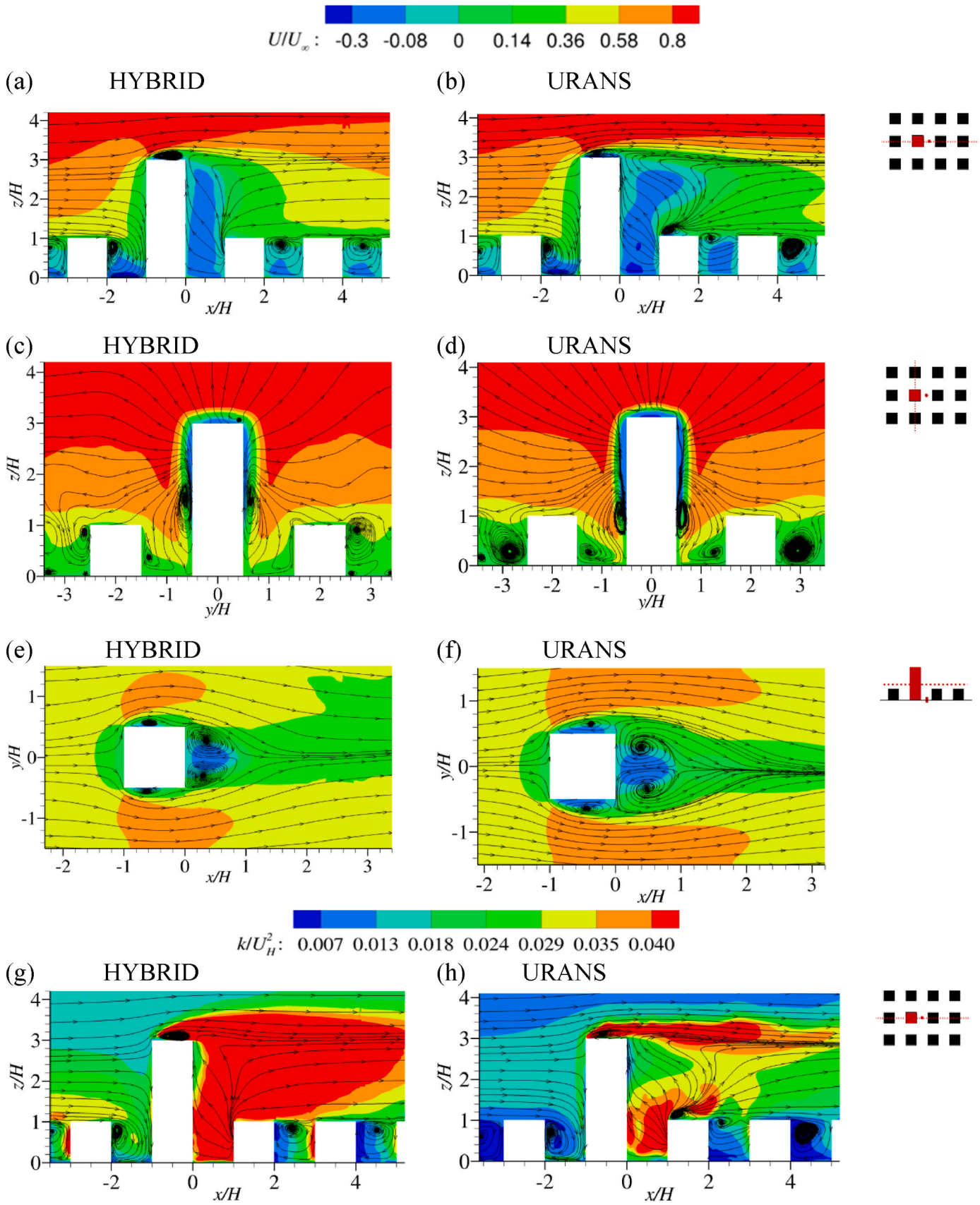


**Fig. 8.** Contours of time-averaged streamwise velocity component and normalized total turbulent kinetic energy with streamlines of time-averaged velocity in different planes. (a), (c), (e), (g) Hybrid results, (b), (d), (f), (h) URANS results.

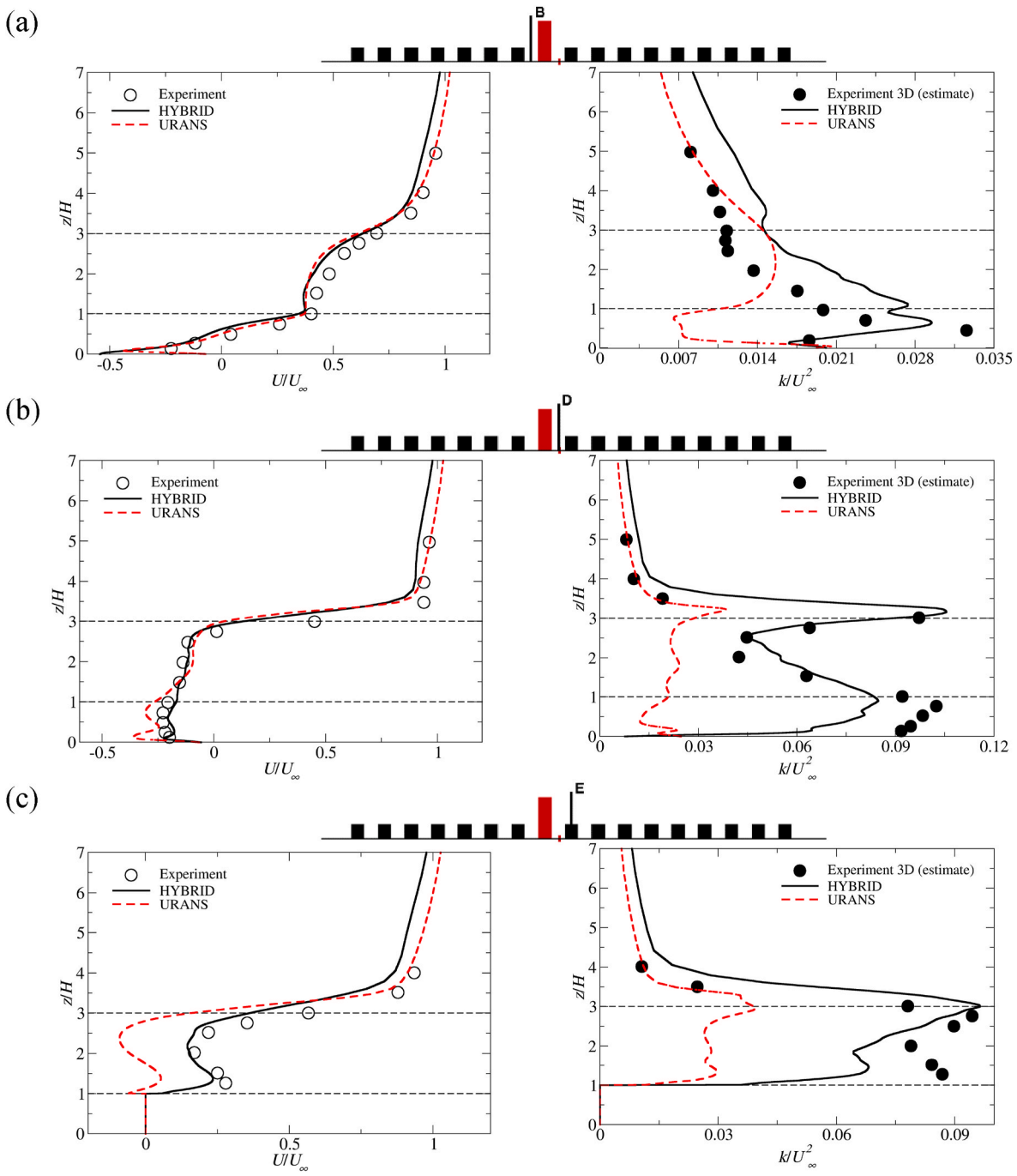


**Fig. 9.** Mean streamwise velocity (left) and total turbulent kinetic energy (right) along the vertical line at several locations in the tower vicinity.

URANS overpredicts the concentration above the source while at location $4H$ from the source both models give good predictions. It is worth mentioning that Kenjereš et al. [63] computed the same case using the $k-\varepsilon$ model and two variants of the hybrid RANS-LES scheme based on the $k-\varepsilon$ model. Although their URANS results resemble ours at certain locations, the overall prediction of the $\zeta-f$ model is significantly better. The same holds for the comparison of the HRL models. The lateral spreading of the pollutant concentration is significantly better predicted by the elliptic-relaxation based HRL model compared to the results of Kenjereš et al. [63].

More insight into the concentration field differences is given in Fig. 11 that shows the fields of the mean concentration of pollutant in the horizontal plane at $z = 0.5H$. Here, we can see some remarkable differences in the predicted pollutant dispersion. The concentration level above the source is significantly higher in the URANS solution compared to HRL as shown in Fig. 10(b). This is related to the URANS overpredicted length of the separation bubble which accumulates and traps the pollutant. The HRL model predicts more lateral spreading of the pollutant and consequently its concentration is smaller downstream of the source compared to the URANS. There is a significant difference in the concentration field in the downstream region far from the source. Beyond $x = 6H$, the URANS predicts significantly higher concentration in a narrow strip behind the source, while the pollutant concentration is smaller in the side regions. This emphasizes the importance of the model capability to accurately capture the wake dynamics for the correct prediction of the concentration field not only close to the source but also in the far field downstream. As it was concluded for the single building, the unsteady separation governed by a vortex-shedding process imposes

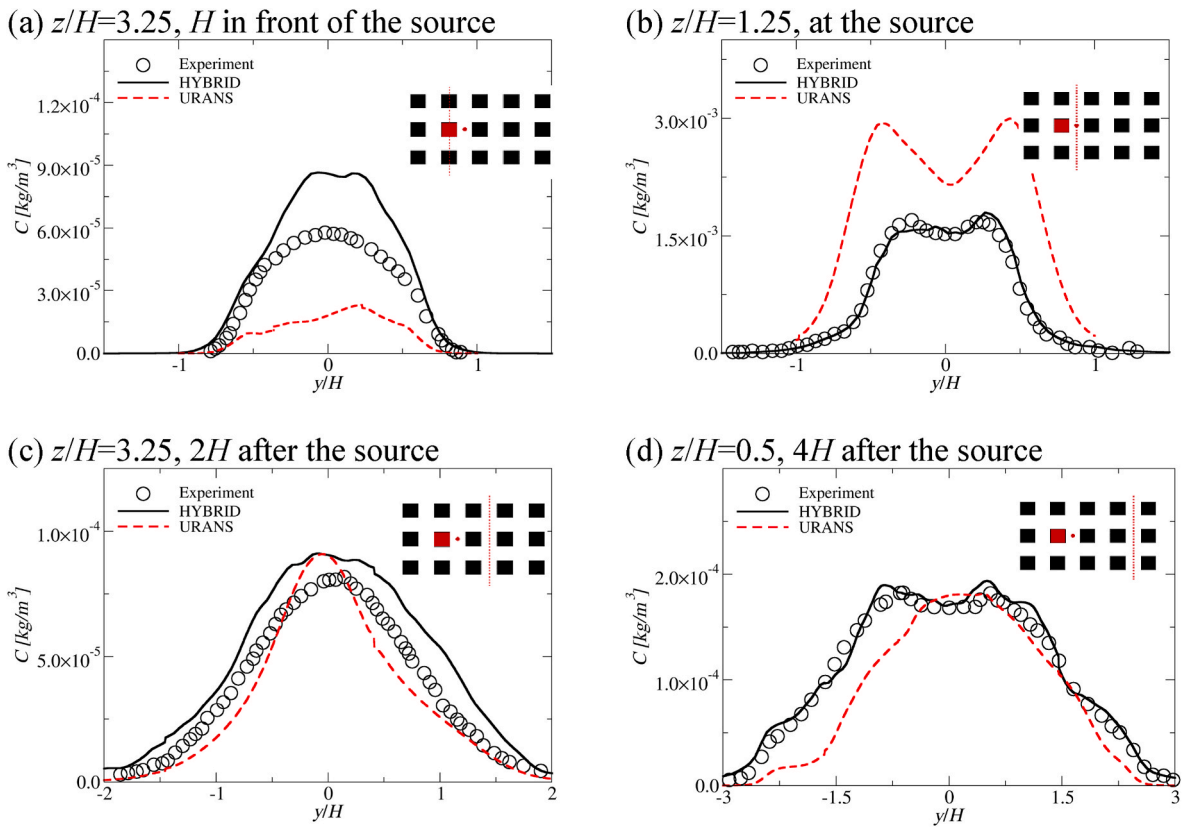


**Fig. 10.** Spanwise profiles of concentration at different heights at several locations: (a) 1$H$ in front of the source (above the tower), (b) at the source, (c) 2$H$ behind the source, and (d) 4$H$ behind the source.

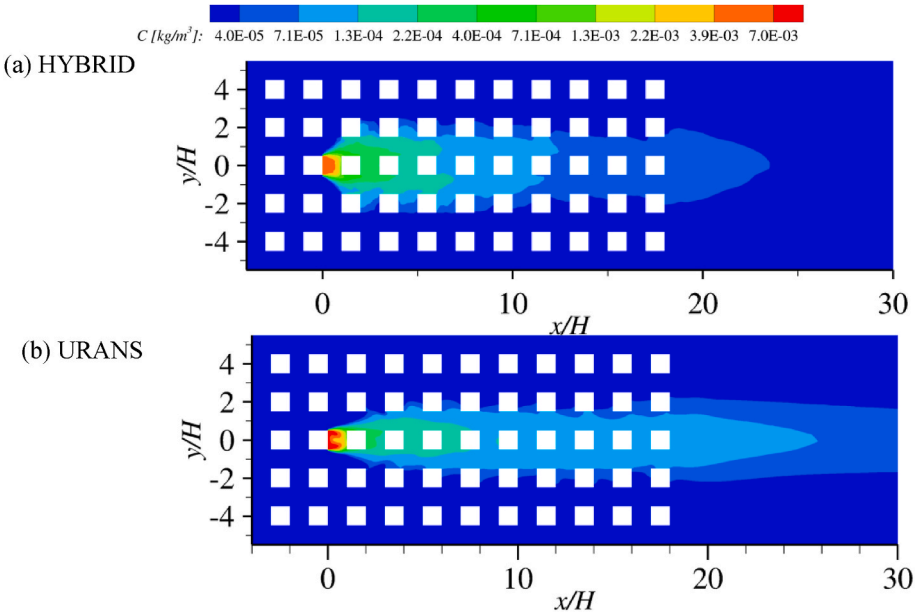


**Fig. 11.** (a) Hybrid and (b) URANS results for the mean pollutant concentration field in the horizontal planes at $z/H = 0.5$. Note that, for clarity, the color bar is defined in an exponential scale. (For interpretation of the references to color in this figure legend, the reader is referred to the Web version of this article.)

a challenge to the URANS model and its ability to accurately predict the wake size and shape, and consequently the correct concentration level both at the pollutant source and the far field. The HRL reproduces the experiment better as shown in Figs. 10 and 11, especially the lateral spreading of the concentration further away from the pollutant source.

### 5.3. Summary on benchmark validations of URANS and hybrid RANS-LES

The stand-alone URANS solution underpredicts the level of the turbulent kinetic energy in the wake in both benchmark cases which leads to an oversized recirculation zone. While the flow and turbulence

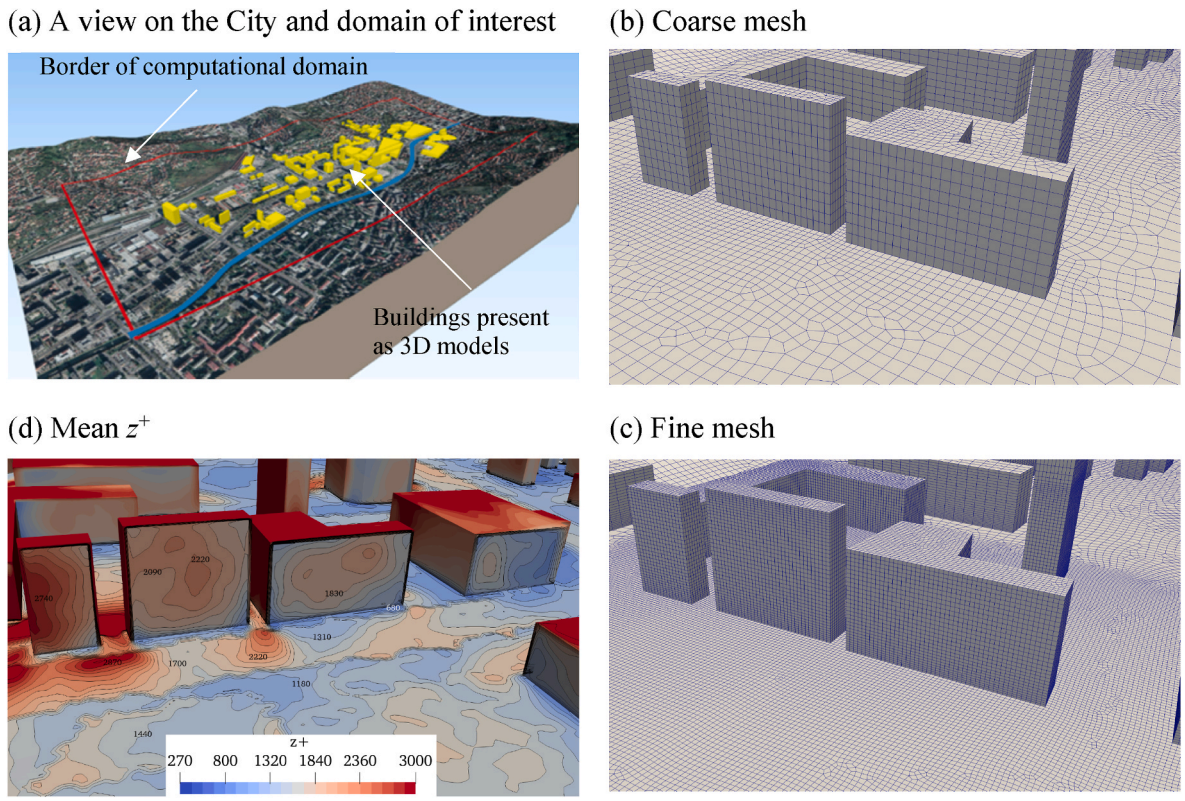


**Fig. 12.** (a) Computational domain marked by the red line with buildings included marked in yellow, and the river marked by a blue stripe, (b), (c) View on computational meshes showing the segment with buildings, (d) Mean value of $z^+$ in the mesh segment obtained on the fine mesh. (For interpretation of the references to color in this figure legend, the reader is referred to the Web version of this article.)

patterns in the impingement regions were reproduced reasonably well in accord with the experiments, the main differences appear thus in the wake region, where URANS tends to overestimate the length of wake. The analysis shows that the main deficiency of the URANS, even when using the elliptic-relaxation approach, is its inability to successfully reproduce the proper three-dimensional dynamics of the shed vortices which are the main carriers of momentum and turbulent kinetic energy behind the objects. Deficiency in the transport of momentum and turbulence from the wake periphery (shear layer) to its center, leads to an underestimation of the turbulent kinetic energy inside the separation bubble that in turn extends its length. As a consequence, the URANS overpredicts the concentration level above the pollutant source and in the narrow strip further downstream, but underpredicts the pollutant lateral spreading. HRL returns more accurately the velocity and turbulence fields which consequently improve the prediction of the concentration field. In the whole, the results of benchmarking illustrate the advantage of the HRL capability to resolve better the organised quasi-periodic vortex structures than URANS, which is a prerequisite for more accurate prediction of the wake dynamics, and consequently, pollutant dispersion in space and time.

## 6. Flow and dispersion of traffic-emitted pollutant in a real urban configuration

We consider now air flow and dispersion of pollutants in a real urban environment. Although URANS showed to perform reasonably well in capturing the main flow features in the two benchmark cases considered, the hybrid RANS-LES showed in a number of details to reproduce just about all flow features in better agreement with the experiment. In view of generally superior performance of the hybrid RANS-LES in the two benchmark cases presented above, the real urban configuration was simulated *only* by the hybrid method. The chosen domain is a downtown segment of the City of Sarajevo, Bosnia and Herzegovina, situated in an elongated valley featured by a river and surrounding hilly terrain with different surface types (residential areas, forests, parks, meadows, areas of low vegetation, etc.). We considered pollution arising from road traffic emission which is dispersed under a mild eastern wind typical for the mid-autumn and spring. The influence of thermal buoyancy, relevant at low wind and especially during windless winter episodes capped by inversion, is here neglected, assumed to be small for the considered scenario. It is noted, however, that modelling of buoyancy-driven flow requires additional care in modelling of the turbulent heat flux, the topic which is beyond the scope of the present publication. The pollutant, the source of which is defined along the main roads in the domain, is treated as a passive scalar. We considered here the $PM_{10}$ as the representative pollutant, emitted from road vehicles with the emission rate estimated from the typical work-day morning traffic density and unit vehicle emission intensity (more details are provided below). Thus, the present study has been aimed primarily at testing the application of the HRL model in real complex urban configuration, and at examining the dispersion patterns for the set scenario with a focus on identifying the occurrence of high-concentration ('hot') pollution spots.

### 6.1. Mesh generating algorithm for urban built environment

The advancement in computational mesh generation techniques allow meshing of complex environmental situations, as demonstrated in Blocken et al. [9]. In spite of these advancements, user intervention might still be needed if we pose particular requirements on the quality of the computational grid. Predominantly hexahedral cells are preferred in the CFD as they make it possible to discretize the conservation equations more accurately than for general cell shapes, and also yield better convergence properties of the resulting systems of equations. The fully automatic procedures to generate hexahedral meshes do not exist for

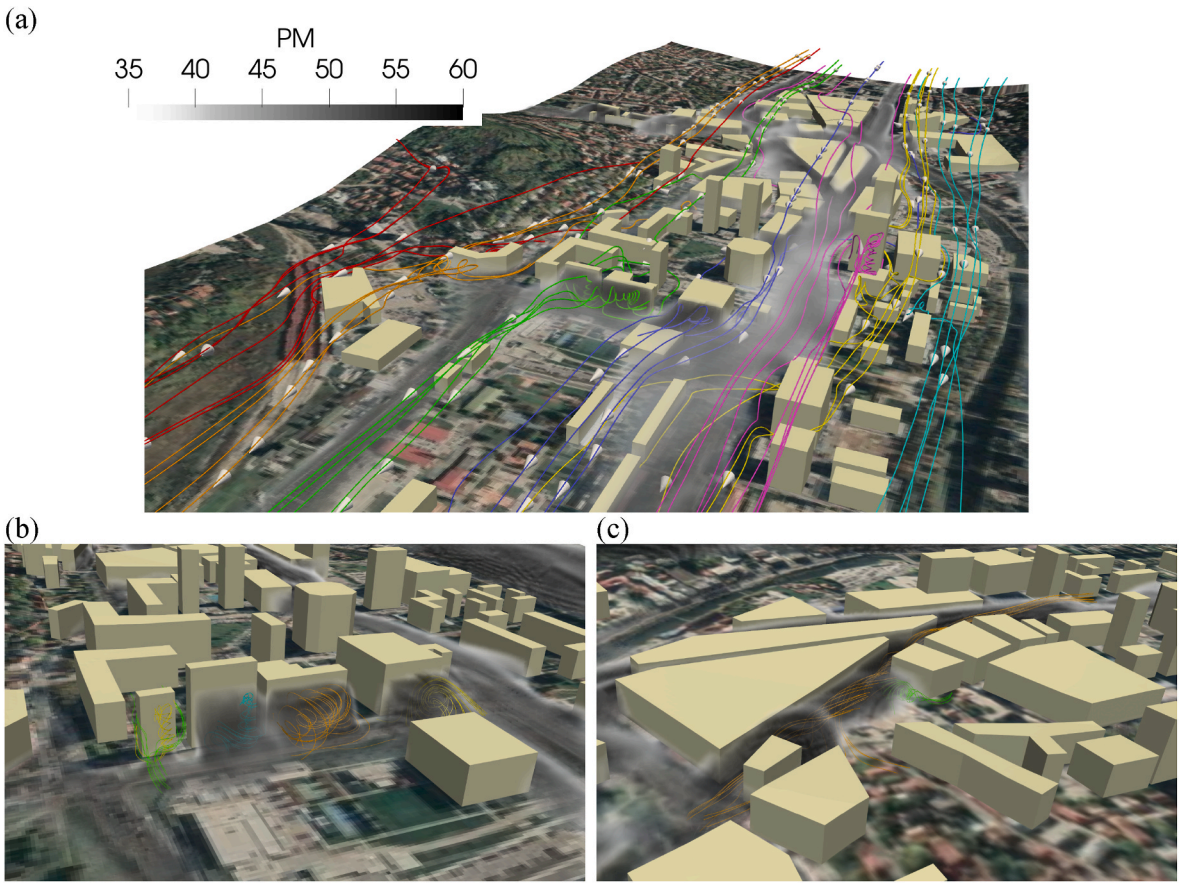


**Fig. 13.** (a) 3D view of pollutant dispersion over the city with representative streamlines (trajectories) colored for visual purpose, (b), (c) Pollutant concentration at two characteristic locations in the city. The colors for streamlines do not have physical meanings and are for a visualization purpose. (For interpretation of the references to color in this figure legend, the reader is referred to the Web version of this article.)

general case, and some manual adjustments might be required to reach the desired grid quality. The question is how much detail/intervention we can afford to dedicate to a particular case being studied. Defining mesh details around each object separately, building by building in case of urban flows, could easily prove to be prohibitively time consuming. An example of such an endeavour is the approach reported by Van Hooff and Blocken [64]. The authors focused on details of the flow around and inside Amsterdam ArenA, and mesh the object with meticulous attention to detail, including even individual openings in the grid while using simpler and coarser cells to represent buildings around it.

In this paper we are not interested in a particular building in the city of Sarajevo, but in a global picture in the whole downtown area. Hence, we resort to a somewhat different, more automatic and less demanding approach within the GMSH mesh generation software, tailored for urban environments. The method proved capable of generating a fast high-quality hexahedra-dominated mesh. The main idea is to create a mesh inside a hexahedral domain, having ground as the bottom face, sky as the upper, and east-west, north and south on the remaining faces of the domain. Since buildings are irregularly placed on the ground, we have also decided to mesh the bottom face with unstructured quadrilateral cells with the algorithm from GMSH and extrude them sky-wise to create layers of hexahedral cells parallel to the ground, resulting in a mesh topologically homogeneous in the vertical direction. On the bottom face, we prescribe ground as one boundary condition (called physical group in GMSH) and each building as an additional boundary condition. The shapes of the buildings are automatically extracted from the Geographic Information System (GIS) file, which describes the City of Sarajevo. The GIS file does not only give coordinates of buildings' edges, but their heights as well. We use these heights when extruding the bottom faces (unstructured quadrilateral) in the vertical direction, in such a way that we extrude individual cells on the ground all the way to the sky face, and cells inside buildings only from their heights to the sky face. Because there is only a finite number of layers in the vertical direction, the heights of the modelled building end up approximated. As the final step, the three-dimensional grid resulting from the above procedure is placed on an STL file which describes the ground elevation. Individual cell layers are clustered to an extent to accommodate the ground. Stepwise, the approach can be summarized as follows:

1. Read GIS file to extract building coordinates and heights and create an input file for GMSH from this information. We wrote an external program for this.
2. Read the input file from step 1 in GMSH software to create a mesh inside a hexahedral domain, with the bottom face having one boundary condition for the ground, and one boundary condition for each building we want to represent, including its height.
3. Create a two-dimensional quadrilateral mesh on the ground from GMSH. This mesh will have boundary conditions in the shape of buildings birds' eye view.
4. Extrude the two-dimensional grid sky-wise in GMSH, making sure that buildings create distinct volumes limited by their heights in three-dimensional grid.
5. Place the resulting three-dimensional grid on an STL file and stretch the vertical node positions where necessary.

Above, steps 2–4 are done automatically in GMSH, and step 5 automatically in T-Flows. If the desired grid quality is not satisfactory (say, some streets are represented with too few cells), we can manually

intervene after step 1 to change the desired cells sizes in the script. That procedure is, however, rarely needed, since minimum cell size is already set to be three times smaller than the smallest distance between any two points in the GIS file. The approach described above gave us high-quality hexahedral meshes with accurate representation of each individual street and building with minimum user intervention.

### 6.2. Computational domain and boundary conditions

The computational domain covers a size of 2.9 km × 1.3 km in East-West and North-South directions. The lowest and highest terrain altitudes in the domain are 527 m and 663 m, respectively, the lowest elevation being in the central part of the domain where most of the buildings are located. Figure 12(a) shows the extent of the computational domain marked by red line while the buildings explicitly modelled are marked in yellow. The total number of buildings presented in the computational domain is 100. The average height of the buildings is 27 m while the tallest building is 87 m. The small objects on the ground such as individual family houses, trees, etc. are accounted for by the roughness model (details provided below). Unlike the ground surface, the buildings' surfaces are treated as smooth walls. The available computer power limits the computations to approximately 6 million cells.

We designed two meshes, denoted as fine and coarse, that differ in the resolution near the ground and the top boundary, aiming to test the mesh resolution impact on the results. The coarse mesh, a segment of which is shown in Fig. 12(b), is totalling to approximately 4.8 million cells with the average cell size in the urban area about 4 m and the centres of the near-wall cells around 1.7 m. The number of cells in the vertical direction is 52, while the domain height in the central part of the domain is around 323 m. The top boundary is located at an elevation of 850 m. The area populated by the buildings is refined compared to the periphery of the computational domain. As seen in Fig. 12(b), the mesh consists mostly of high-quality hexahedral cells with very few cells of irregular shape. The fine mesh, shown in Fig. 12(c), has a finer resolution in the near-ground/wall region with the centres of the near-wall cells around 0.3 m and 60 cells in the ground-normal direction. The size of the computational domain is the same as in the coarse mesh, but with the top boundary moved to 980 m elevation. The new position of the top boundary gives the domain height in the central region of 453 m. The area of interest (Halid Kajtaz Street) shown in Fig. 12(c) is significantly refined compared to the coarse mesh while the rest of the domain has the mesh resolution in the ground-parallel directions comparable to the coarse mesh. The value of $z^+$ obtained on the fine mesh varies between 270 and 3000, Fig. 12(d), while the coarse mesh has $z^+$ typically around 1500–8000. This is not surprising knowing that the Reynolds number of the flow is order of $10^7$. The vertical extension of the domain for both meshes satisfies the condition that the maximum blockage is less than 3% (Baetke et al., [65]), where blockage is defined as the ratio of projected area of the structures in flow direction to the cross-sectional area of the domain at the location of the structures.

An easterly wind of 1.8 m/s magnitude is assumed and imposed as a fully developed turbulent flow at the inflow boundary. The inflow velocity field is perturbed by the vortex-generated method (Oh et al. [66]) aiming to generate three-dimensional, unsteady inflow condition. The zero-gradient boundary condition is applied at the lateral sides and top, while pressure boundary condition is imposed at the outflow. The effect of natural (forests, rivers, grass fields) and man-made (buildings, houses, bridges, roads) ground obstacles in the surrounding of the area are represented by the roughness model (Section 2). The roughness zones are extracted by using Geographic Information System (GIS) software, then $z_0$ values are interpolated on the surface. We defined four terrain types with the corresponding values of $z_0$ adopted from the recommendation of Wieringa [56] as follows: river $z_0 = 0.005$ m, residential area (private houses) $z_0 = 1.0$ m, green fields $z_0 = 0.015$ m, forest $z_0 = 1.0$ m, roads $z_0 = 0.15$ m.

For the computation of a real city case, the same numerics is used as in the benchmark cases. The time step is set to $\Delta t = 0.5$ s which ensured the CFL number around 1. The simulations were conducted on 36 processors with the total computational time around 11 days (9000 CPU hours) for the fine mesh.

### 6.3. Pollutant source

We considered $PM_{10}$ as a representative pollutant since the traffic-related emissions of $PM_{10}$ is the most reported in the literature (Peitzmeier et al. [67]). The way to estimate the line source from the traffic is not straightforward, and it varies in the literature. We estimated the line source intensity in Eq. (3) by combining the number of vehicles per hour $N_V$ [V/h] (data obtained from the local authorities), mass of emitted particles per kilometre per vehicle $E_Q$ [g/(km V)], $L$ [m] length of road and number of lanes $N_{lanes}$ for each street considered as follows

$$S_c'' = \rho E_Q N_V L \Big/ (3.6 N_{lanes}) \quad \left[\frac{\mu g}{m^3} \Big/ s\right] \tag{21}$$

The number of vehicles varies during the day, with the peak values lasting for a few hours and occurring typically in mornings and afternoons. The considered scenario is focusing on a rush hour situation when the number of vehicles reaches the maximum (2000 vehicles per hour) on the main road, which remains constant for 2–3 h of real time. The emission per vehicle, defined per kilometre, greatly depends on the vehicle type (diesel or gasoline, passenger car or trucks, etc.) and age, as well as the mode of driving (stop and go versus smooth flow of traffic). We adopted the source intensity value of 0.0216 [g/(km V)] considering the average age of vehicles in Sarajevo, the fact that the diesel engine vehicles dominate, and stop-and-go mode of driving. The adopted source intensity for the local streets is between 36% and 25% of the source intensity for the main street depending on the estimated traffic frequency. As the considered computational domain is in the city centre, it is assumed that the incoming air into the solution domain has a $PM_{10}$ concentration of 30. This is a likely scenario when the buoyancy driven motion is small. The variables defined at the boundaries are kept steady during the computations that were conducted in an unsteady mode.

### 6.4. Results

Figure 13(a) shows a three-dimensional view of the pollutant dispersion over the city. As expected, the highest concentration appears along the main roads which are the pollutant source. However, the concentration varies quite a lot both in space and time. The concentration field reveals that the pollution hot spots appear in two characteristic regions. The first is the region where the strong pollutant source (roads) overlap with the massive recirculation zones formed in the wake of large objects on the ground. This is a case in the Halid Kajtaz Street shown in Fig. 13(b), where large recirculation zones are formed on the leeward side of the relatively tall buildings with their larger sides oriented perpendicularly to the dominant wind direction. The pollutant is accumulated in the wake and transported up towards the building top. The second critical regions are the street canyons where poor ventilation and strong emissions of pollutants from the traffic lead to high concentrations as shown in Fig. 13(c).

The mean velocity vectors and concentration contours in vertical cross-sections at these two locations are shown in Fig. 14(b) and (c). The cross-section shown in Fig. 14(b) contains two street canyons with similar configurations. The region of high concentration level extends up to the heights of the buildings that form the street canyons. However, the area of high pollution is smaller in the street canyon on right. The vicinity of an open area upstream of the right-hand side street canyon, Fig. 14(a), most likely enhances the ventilation and helps reducing the concentration level. The cross-section shown in Fig. 14(c) is placed in leeward side of the buildings orientated perpendicular to the dominant wind direction. The imprints of the separation bubbles formed in the

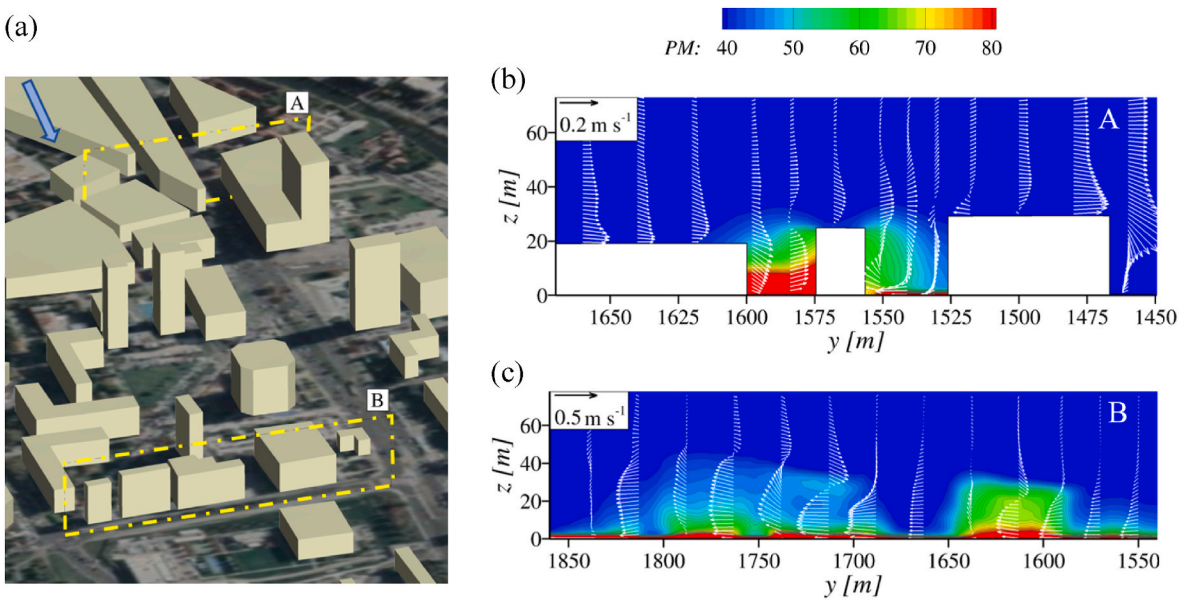


**Fig. 14.** (a) The locations in the city where the cross-section fields are extracted. The blue arrow indicates the prevailing wind direction and yellow squares indicate positions of cross sections. (b), (c) Mean velocity vectors (in-plain components) and concentration contours in vertical cross-sections at two locations in the city. (For interpretation of the references to color in this figure legend, the reader is referred to the Web version of this article.)

wake of the buildings are marked by the high concentration areas. The wake contours behind the large building on the right correspond relatively close with the region of high concentration behind the building, extending up to its top. The ground layer of high concentration behind the other buildings of similar heights is, however, thinner. The vector field indicates a higher lateral wind in the region of lower concentration presumably generated by the jets formed in the narrow passages between the buildings. More intense mixing is reducing the concentration level on the left side of the cross-section plain.

We look further into the connection between the velocity field, turbulent kinetic energy, and the pollutant concentration PM. Figure 15 compares the profiles of the streamwise velocity component, turbulent kinetic energy, and concentration along the vertical lines at several locations in the City downtown region obtained on the coarse and fine meshes. We first comment on the comparisons of the results obtained on two different meshes. Even though the cell-centres of the wall-adjacent cells in the coarse mesh are much further from the ground ($z_P = 1.7$ m) compared to the fine mesh ($z_P = 0.3$ m), the results are remarkably similar. The most profound difference appears on the location B placed in the vicinity of the large building on the right. The coarser mesh returns flow separation close to the wall (negative velocity) while the finer mesh predicts a small positive velocity. The most probable reason for this discrepancy is the overprediction of the horseshoe vortex size on the coarser mesh to which the prediction of flow impingement is known to be sensitive. This assumption is supported by the results for the turbulent kinetic energy where the coarser mesh produces significantly higher values close to the wall, a deviation typical for the impingement area obtained on a coarse mesh. The concentration values close to the ground at location B are similar for two meshes even though there is a discrepancy in the velocity and turbulent kinetic energy values. Location B is placed relatively far from the main pollution sources (two parallel main roads), and at the edge of the smaller road located downstream. The pollutant at location B is mainly convected from the upstream region. In the case of the coarser mesh, the flow separation that occurs on the ground tends to increase the pollutant concentration, but at the same time the local mixing is intensified by the high intensity of turbulence reducing the concentration close to the ground. This results in the concentration level that is similar to the value obtained on the fine mesh where the increase in the pollutant close to the ground is due to slowing down of air as it approaches the building downstream.

The other three locations show very similar velocity and concentration profiles, and to a less extent the profiles of the turbulent kinetic energy. The flow on location A, placed on the lee side of the tall building, is dominated by the massive separation which is resolved by the HRL model. Even though the mesh is relatively coarse, it seems to be of sufficient resolution for capturing the main dynamics of flow separation. The matching of the profiles on the two other locations, C and D, are less surprising as they are placed on the main road, in the region outside the wakes of the neighboring buildings. As the gradients of the computed variables are high close to the wall, the near-wall mesh resolution could have a strong impact on the values in the wall vicinity. This is reflected in the pollutant distribution close to the ground at locations B and D where the concentration is significantly lower on the coarse mesh.

We turn now our focus on the concentration profiles shown in Fig. 15 (d). All the profiles are extracted at the locations along the pollution sources (roads). The highest concentration appears at location A (the site also indicated in Fig. 13(b)), characterized by negative (backflow) velocity near the ground due to massive separation. The high values of pollutant concentration (>50 $PM_{10}$) extend up to the height of 35 m which roughly coincides with the height of the separation bubble forming the building wake. This value is almost constant in the region from 15 to 35 m from the ground, after which it rapidly decreases to the background concentration value of 30 $PM_{10}$. Near the ground, at the pedestrian level, the pollutant concentration reaches values as high as 80 $PM_{10}$. It is interesting to observe the concentration levels at three other locations, B, D and C. Even though the velocity profiles are similar at these three locations, the concentration levels differ quite a lot, with 37 $PM_{10}$, 47 $PM_{10}$ and 55 $PM_{10}$ at B, D and C respectively. What makes a difference here is the level of turbulence, represented by the turbulent kinetic energy close to the ground. The highest and lowest level of the turbulent kinetic energy corresponds to the lowest and highest concentration levels.

### 6.5. *Comments on the wall functions boundary conditions*

The presented results demonstrate the strong influence of the shape, height, and position of the buildings on the local pollutant distribution. Understanding the flow structures dynamics and morphology, which are

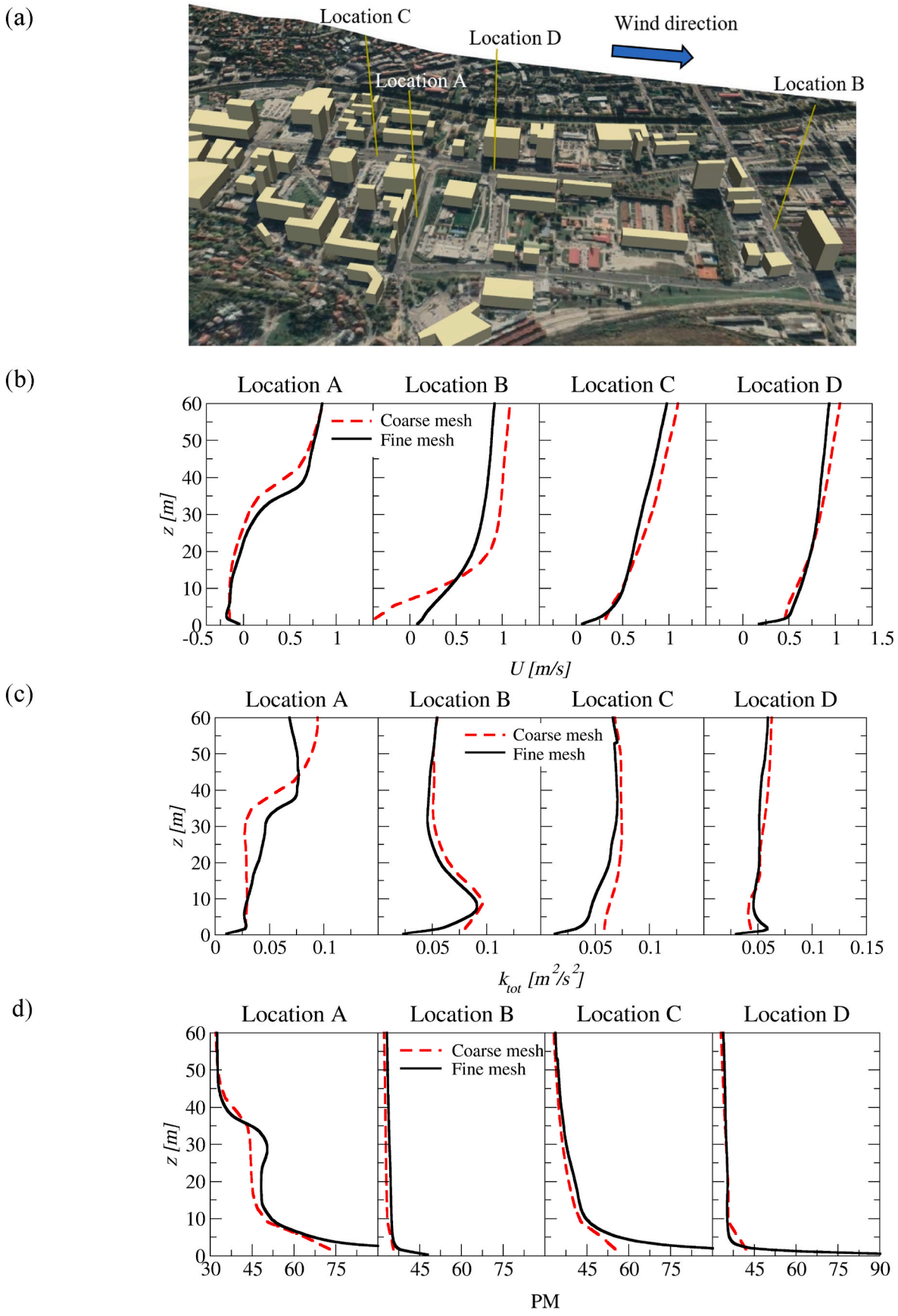


**Fig. 15.** (a) The locations in the city where the profiles are extracted. Profiles of (b) streamwise velocity, (c) turbulent kinetic energy, and (d) PM concentration along vertical lines at four locations in the domain.

by large determined by the objects on the ground, it is crucial for understanding the way the pollutants are transported, dispersed, and distributed in urban configurations. To illustrate the extent of the flow non-equilibrium in the ground-adjacent layer and beyond, as well as to indicate the location of the wall-nearest grid point in the fine and coarse mesh used here, Fig. 16 shows the tangential velocity $\sqrt{U^2+V^2}$ profiles at four locations in the common semi-logarithmic plot, compared with the standard equilibrium log-law plots for the smooth and the rough surfaces at the location considered. Figure 16(a) shows the velocity profiles for the fine mesh at four locations with an indicator of the RANS-LES virtual (seamless) interface. At all locations, the velocity profiles follow the log-law line for a fully rough wall. The wall/ground-adjacent RANS region, defined by $\alpha = 1$, contains 7 cells in the near-wall region, after which the model gradually transits to LES with the dynamic Smagorinsky SGS model.

In Fig. 16(b), (c) the tangential velocity profiles from the fine and coarse mesh results are compared at locations B and D. The velocities in the wall-adjacent cells are similar although the differences are present in the profiles' shapes especially at location B. The location B is in the separation bubble of the building wake, in the region where the fine mesh is considerable finer compared to the coarse mesh. Thus, it is not surprising that the differences are present.

## 7. Conclusions

We conducted computations of air flow and pollutant dispersion in idealized and real urban configurations using two turbulence modelling approaches, a stand-alone URANS and a hybrid RANS-LES (HRL). Both approaches employ the same elliptic-relaxation $k-\varepsilon-\zeta-f$ eddy-viscosity RANS model, which for URANS is used in the whole computational domain, whereas for HRL only in the ground/wall-adjacent region with the outer flow entrusted to the dynamic Smagorinsky LES. For the two benchmark cases considered the elliptic-relaxation based URANS predicts the main flow and pollutant dispersion fairly well in accord with the experimental data, notably better than when using the standard $k-\varepsilon$, especially in the steady mode. However, the HRL approach (also benefiting from the elliptic-relaxation concept) shows superior predictions in both benchmark cases. The superior performance of HRL compared to URANS is attributed to better resolution of the intrinsic unsteady dynamics of the quasi-periodic organized vortex structures shed from objects, thus capturing better the time-resolved filtered (in the LES region) and ensemble-averaged (in the URANS region) turbulent stress field to complement the stochastic contributions provided by the RANS turbulence model. This results in a better prediction of the total (resolved plus modelled) turbulent kinetic energy and turbulent stress, as well as the characteristic turbulence scales, and thus a more realistic mixing in the separation zones/buildings' wakes which are susceptible to accumulation of the pollutants. The lateral spreading of the pollutant in idealized city is significantly underpredicted by URANS in the downstream region far from the point source. It is shown, however, that the URANS solution can be improved if an unsteady inflow from precursor solutions is imposed to speed up the development of flow instabilities inherent to flows around bluff bodies.

The real city computation with the pollutant emitted from the traffic shows highly versatile flow patterns generated by an interplay of neighboring objects and the terrain. The massive separations that occur behind the buildings, impingement zones, acceleration and deceleration of the flow dictated by the urban morphology generate a complex picture of the pollutant dispersion. The pollutant concentration significantly varies in space and time with pollution hot spots identified in the region of street canyon and massive separations that overlap with the strong pollution sources on the ground. The results confirm the unique potential of CFD when used with the adequate turbulence models and wall/ground treatment, to accurately predict dispersion of air pollutant

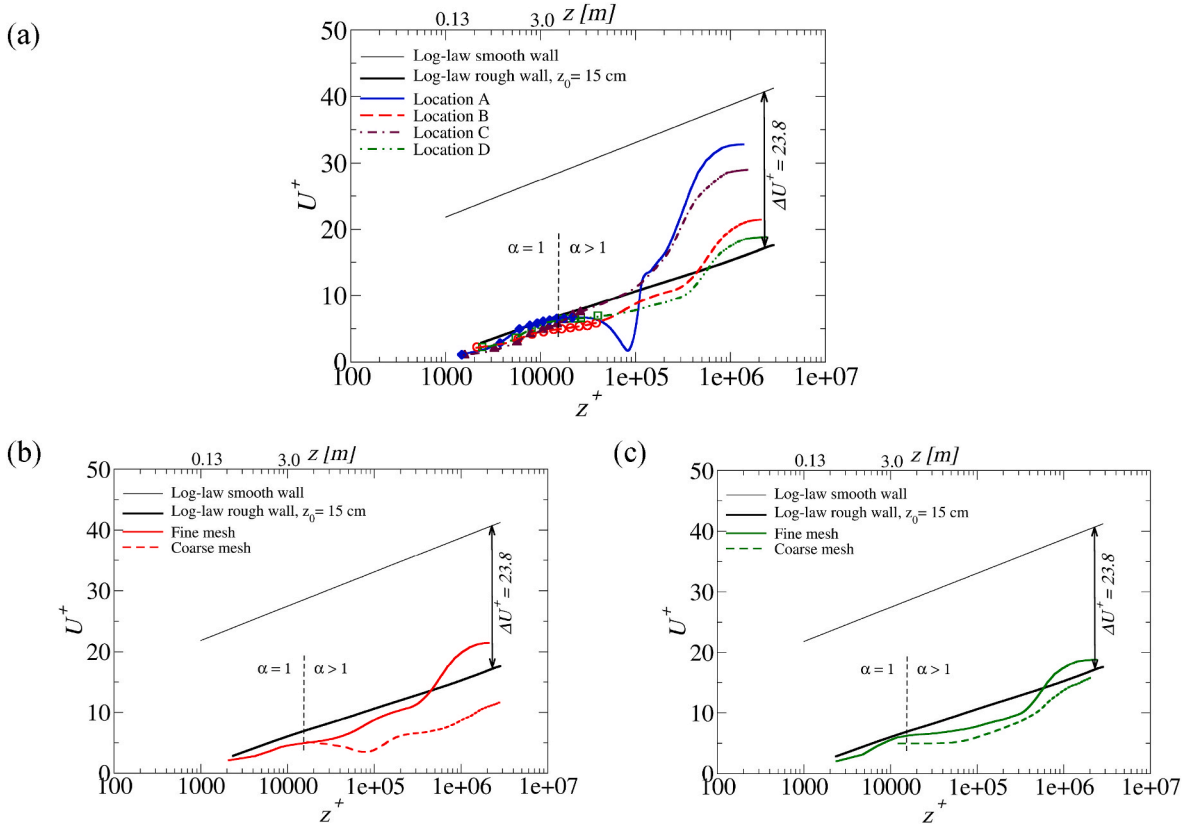


**Fig. 16.** (a) Tangential velocity profiles at four locations in the semi-log plot compared to log-law. (b), (c) comparison of tangential velocity profiles in semi-log plot at locations B and D obtained on the fine and course mesh. α is defined by Eq. (13).

in the urban configurations, but also warn on consequences of using too simplistic modelling approach.

Another contribution of the paper is an efficient semi-automated fast method for generation of computational mesh for real-city urban environments. The method offers a possibility to quickly add/remove/replace objects on the ground.

## Funding

This research did not receive any specific grant from funding agencies in the public, commercial, or not-for-profit sectors.

## CRediT authorship contribution statement

**Muhamed Hadžiabdić:** Writing – original draft, Methodology, Formal analysis, Conceptualization. **Mahir Hafizović:** Writing – review & editing, Visualization, Formal analysis. **Bojan Ničeno:** Software, Methodology. **Kemal Hanjalić:** Writing – review & editing, Methodology, Conceptualization.

## Declaration of competing interest

The authors declare that they have no known competing financial interests or personal relationships that could have appeared to influence the work reported in this paper.

## Acknowledgements

We thank the Ministry of Science, Higher Education and Youth of Sarajevo Canton for supporting the research published in this paper. The computational resources are provided by International University of Sarajevo (Sarajevo) and Enova – Consultants and Engineers (Sarajevo).

## References

[1] Y. Tominaga, T. Stathopoulos, CFD simulation of near-field pollutant dispersion in the urban environment: a review of current modeling techniques, Atmos. Environ. 79 (2013) 716–730.
[2] S. Di Sabatino, R. Buccolieri, P. Salizzoni, Recent advancements in numerical modelling of flow and dispersion in urban areas: a short review, Int. J. Environ. Pollut. 52 (3–4) (2013) 172–191.
[3] B. Blocken, 50 years of computational wind engineering: past, present and future, J. Wind Eng. Ind. Aerod. 129 (2014) 69–102.
[4] B. Blocken, Computational Fluid Dynamics for Urban Physics: importance, scales, possibilities, limitations and ten tips and tricks towards accurate and reliable simulations, Build. Environ. 91 (2015) 219–245.
[5] R. Ramponi, B. Blocken, CFD simulation of cross-ventilation for a generic isolated building: impact of computational parameters, Build. Environ. 53 (2012) 34–48.
[6] Y. Tominaga, Flow around a high-rise building using steady and unsteady RANS CFD: effect of large-scale fluctuations on the velocity statistics, J. Wind Eng. Ind. Aerod. 142 (2015) 93–103.
[7] J. Liu, J. Niu, CFD simulation of the wind environment around an isolated high-rise building: an evaluation of SRANS, LES and DES models, Build. Environ. 96 (2016) 91–106.
[8] T. Van Hooff, B. Blocken, Y. Tominaga, On the accuracy of CFD simulations of cross-ventilation flows for a generic isolated building: comparison of RANS, LES and experiments, Build. Environ. 114 (2017) 148–165.
[9] B. Blocken, T. Stathopoulos, J. Carmeliet, J.L.M. Hensen, Application of computational fluid dynamics in building performance simulation for the outdoor environment: an overview, J. Build. Perform. Simul. 4 (2) (2011) 157–184.
[10] R. Yoshie, G. Jiang, T. Shirasawa, J. Chung, CFD simulations of gas dispersion around high-rise building in non-isothermal boundary layer, J. Wind Eng. Ind. Aerod. 99 (4) (2011) 279–288.
[11] Y. Tominaga, T. Stathopoulos, Steady and unsteady RANS simulations of pollutant dispersion around isolated cubical buildings: effect of large-scale fluctuations on the concentration field, J. Wind Eng. Ind. Aerod. 165 (2017) 23–33.
[12] Y. Tominaga, S.I. Akabayashi, T. Kitahara, Y. Arinami, Air flow around isolated gable-roof buildings with different roof pitches: wind tunnel experiments and CFD simulations, Build. Environ. 84 (2015) 204–213.
[13] Y. Tominaga, B. Blocken, Wind tunnel analysis of flow and dispersion in cross-ventilated isolated buildings: impact of opening positions, J. Wind Eng. Ind. Aerod. 155 (2016) 74–88.
[14] T. Van Druenen, T. Van Hooff, H. Montazeri, B. Blocken, CFD evaluation of building geometry modifications to reduce pedestrian-level wind speed, Build. Environ. 163 (2019), 106293.
[15] R. Yoshie, A. Mochida, Y. Tominaga, H. Kataoka, K. Harimoto, T. Nozu, T. Shirasawa, Cooperative project for CFD prediction of pedestrian wind environment in the Architectural Institute of Japan, J. Wind Eng. Ind. Aerod. 95 (9–11) (2007) 1551–1578.
[16] Y. Tominaga, A. Mochida, S. Murakami, S. Sawaki, Comparison of various revised k–ε models and LES applied to flow around a high-rise building model with 1:1:2 shape placed within the surface boundary layer, J. Wind Eng. Ind. Aerod. 96 (4) (2008) 389–411.
[17] S. Branford, O. Coceal, T.G. Thomas, S.E. Belcher, Dispersion of a point-source release of a passive scalar through an urban-like array for different wind directions, Boundary-Layer Meteorol. 139 (3) (2011) 367–394.
[18] O. Coceal, E.V. Goulart, S. Branford, T.G. Thomas, S.E. Belcher, Flow structure and near-field dispersion in arrays of building-like obstacles, J. Wind Eng. Ind. Aerod. 125 (2014) 52–68.
[19] V. Fuka, Z.T. Xie, I.P. Castro, P. Hayden, M. Carpentieri, A.G. Robins, Scalar fluxes near a tall building in an aligned array of rectangular buildings, Boundary-Layer Meteorol. 167 (1) (2018) 53–76.
[20] J.M. Santos, N.C. Reis, I.P. Castro, E.V. Goulart, Z.T. Xie, Using large-eddy simulation and wind-tunnel data to investigate peak-to-mean concentration ratios in an urban environment, Boundary-Layer Meteorol. 172 (3) (2019) 333–350.
[21] J.O. Cheung, C.H. Liu, CFD simulations of natural ventilation behaviour in high-rise buildings in regular and staggered arrangements at various spacings, Energy Build. 43 (5) (2011) 1149–1158.
[22] I.P. Castro, Z.T. Xie, V. Fuka, A.G. Robins, M. Carpentieri, P. Hayden, O. Coceal, Measurements and computations of flow in an urban street system, Boundary-Layer Meteorol. 162 (2) (2017) 207–230.
[23] Z. Tong, Y. Chen, A. Malkawi, Defining the Influence Region in neighborhood-scale CFD simulations for natural ventilation design, Appl. Energy 182 (2016) 625–633.
[24] E.R. Meinders, K. Hanjalić, Vortex structure and heat transfer in turbulent flow over a wall-mounted matrix of cubes, Int. J. Heat Fluid Flow 20 (3) (1999) 255–267.
[25] O. Coceal, T.G. Thomas, I.P. Castro, S.E. Belcher, Mean flow and turbulence statistics over groups of urban-like cubical obstacles, Boundary-Layer Meteorol. 121 (3) (2006) 491–519.
[26] Z.T. Xie, O. Coceal, I.P. Castro, Large-eddy simulation of flows over random urban-like obstacles, Boundary-Layer Meteorol. 129 (1) (2008) 1–23.
[27] M. Carpentieri, A.G. Robins, Influence of urban morphology on air flow over building arrays, J. Wind Eng. Ind. Aerod. 145 (2015) 61–74.
[28] R. Ramponi, B. Blocken, B. Laura, W.D. Janssen, CFD simulation of outdoor ventilation of generic urban configurations with different urban densities and equal and unequal street widths, Build. Environ. 92 (2015) 152–166.
[29] B. Blocken, J. Carmeliet, Pedestrian wind conditions at outdoor platforms in a high-rise apartment building: generic sub-configuration validation, wind comfort assessment and uncertainty issues, Wind Struct. 11 (1) (2008) 51–70.
[30] Z.T. Xie, I.P. Castro, Large-eddy simulation for flow and dispersion in urban streets, Atmos. Environ. 43 (13) (2009) 2174–2185.
[31] P. Gousseau, B. Blocken, T. Stathopoulos, G.J.F. Van Heijst, CFD simulation of near-field pollutant dispersion on a high-resolution grid: a case study by LES and RANS for a building group in downtown Montreal, Atmos. Environ. 45 (2) (2011) 428–438.
[32] B. Blocken, W.D. Janssen, T. van Hooff, CFD simulation for pedestrian wind comfort and wind safety in urban areas: general decision framework and case study for the Eindhoven University campus, Environ. Model. Software 30 (2012) 15–34.
[33] Y. Toparlar, B. Blocken, P.V. Vos, G.J.F. Van Heijst, W.D. Janssen, T. van Hooff, H. J.P. Timmermans, CFD simulation and validation of urban microclimate: a case study for Bergpolder Zuid, Rotterdam, Build. Environ. 83 (2015) 79–90.
[34] Z. Gao, R. Bresson, Y. Qu, M. Milliez, C. de Munck, B. Carissimo, High resolution unsteady RANS simulation of wind, thermal effects and pollution dispersion for studying urban renewal scenarios in a neighborhood of Toulouse, Urban Clim. 23 (2018) 114–130.
[35] N. Antoniou, H. Montazeri, M. Neophytou, B. Blocken, CFD simulation of urban microclimate: validation using high-resolution field measurements, Sci. Total Environ. 695 (2019) 133743.
[36] K. Hanjalić, M. Popovac, M. Hadžiabdić, A robust near-wall elliptic-relaxation eddy-viscosity turbulence model for CFD, Int. J. Heat Fluid Flow 25 (6) (2004) 1047–1051.
[37] B. Ničeno, An Unstructured Parallel Algorithm for Large Eddy and Conjugate Heat Transfer Simulations, PhD thesis, Delft University of Technology, Delft, the Netherlands, 2001.
[38] B. Ničeno, K. Hanjalić, Unstructured large-eddy and conjugate heat transfer simulations of wall-bounded flows, in: S. Sunden, M. Faghri (Eds.), Modelling and Simulation of Turbulent Heat Transfer, WIT Press, USA, 2005, pp. 35–76.
[39] M. Hadžiabdić, LES, RANS and Combined Simulation of Impinging Flows and Heat Transfer, PhD thesis, Delft University of Technology, Delft, The Netherlands, 2006.
[40] G. Delibra, K. Hanjalic, D. Borello, F. Rispoli, Vortex structures and heat transfer in a wall bounded pin matrix: LES with a RANS wall treatment, Int. J. Heat Fluid Flow 31 (5) (2010) 740–753.
[41] D. Borello, A. Salvagni, K. Hanjalić, Effects of rotation on flow in an asymmetric rib-roughened duct: LES study, Int. J. Heat Fluid Flow 55 (2015) 104–119.
[42] E. Palkin, M. Hadžiabdić, R. Mullyadzhanov, K. Hanjalić, Control of flow around a cylinder by rotary oscillations at a high subcritical Reynolds number, J. Fluid Mech. 855 (2018) 236–266.
[43] M. Van Reeuwijk, M. Hadžiabdić, Modelling high Schmidt number turbulent mass transfer, Int. J. Heat Fluid Flow 51 (2015) 42–49.

[44] L. Temmerman, M. Hadžiabdić, M.A. Leschziner, K. Hanjalić, A hybrid two-layer URANS–LES approach for large eddy simulation at high Reynolds numbers, Int. J. Heat Fluid Flow 26 (2) (2005) 173–190.
[45] E. Palkin, M. Hadžiabdić, R. Mullyadzhanov, K. Hanjalić, Scrutinizing URANS in shedding flows: the case of cylinder in cross-flow in the subcritical regime, Flow, Turbul. Combust. 97 (2016) 1017–1046.
[46] P.A. Durbin, Near-wall turbulence closure modeling without "damping functions, Theor. Comput. Fluid Dynam. 3 (1) (1991) 1–13.
[47] M. Lateb, C. Masson, T. Stathopoulos, C. Bédard, Comparison of various types of k-ε models for pollutant emissions around a two-building configurations, J. Wind Eng. Ind. Aerod. 115 (2013) 9–21.
[48] Y. Tominaga, T. Stathopoulos, Numerical simulation of dispersion around an isolated cubic building: comparison of various types of k–ε models, Atmos. Environ. 43 (2009) 3200–3210.
[49] P.A. Durbin, On the k –ε stagnation point anomaly, Int. J. Heat Fluid Flow 17 (1996) 89–90.
[50] K. Hanjalić, Will RANS survive LES? A view of perspectives, ASME J. Fluids Engineering 127 (2005) 831–839, 2005.
[51] M. Hadžiabdić, K. Hanjalić, Elliptic-relaxation hybrid RANS-LES (ER-HRL) for complex wall-bounded fluid and heat flows, ERCOFTAC Bulletin 121 (2020) 17–24.
[52] P.A. Durbin, G. Medic, J.M. Seo, J.K. Eaton, S. Song, Rough wall modification of two-layer k−ε, J. Fluid Eng. 123 (1) (2001) 16–21.
[53] B. Blocken, J. Carmeliet, T. Stathopoulos, CFD evaluation of wind speed conditions in passages between parallel buildings—effect of wall-function roughness modifications for the atmospheric boundary layer flow, J. Wind Eng. Ind. Aerod. 95 (9–11) (2007) 941–962.
[54] A. Parente, C. Gorlé, J. van Beeck, C. Benocci, A comprehensive modelling approach for the neutral atmospheric boundary layer: consistent inflow conditions, wall function and turbulence model, Boundary-Layer Meteorol. 140 (3) (2011) 411–428.
[55] Y. Toparlar, B. Blocken, B. Maiheu, G. van Heijst, CFD simulation of the near-neutral a mospheric boundary layer: new temperature inlet profile consistent with wall functions, J. Wind Eng. Ind. Aerod. 191 (2019) 91–102, 2019, 0167–6105.
[56] J. Wieringa, Updating the Davenport roughness classification, J. Wind Eng. Ind. Aerod. 41 (1–3) (1992) 357–368.
[57] M. Popovac, K. Hanjalić, Compound wall treatment for RANS computation of complex turbulent flows and heat transfer, Flow, Turbul. Combust. 78 (2) (2007) 177.
[58] K. Hanjalić, B.E. Launder, Modelling Turbulence in Engineering and the Environment, Cambridge University Press, Cambridge, UK, 2011 (second edition in press).
[59] C. Geuzaine, J.F. Remacle, Gmsh: a 3-D finite element mesh generator with built-in pre-and post-processing facilities, Int. J. Numer. Methods Eng. 79 (11) (2009) 1309–1331.
[60] P.H. Gaskell, A. Lau, Curvature-compensated convective transport: SMART, a new boundedness-preserving transport algorithm, Int. J. Numer. Methods Fluid. 8 (6) (1988) 617–641.
[61] T. Hilderman, R. Chong, A Laboratory Study of Momentum and Passive Scalar Transport and Diffusion within and above a Model Urban Canopy, CR 2008-025, Coanda Research & Development Corporation, Defence R&D Suffield, Canada, 2007.
[62] J. Franke, A. Hellsten, H. Schlünzen, B. Carissimo, Best Practice Guideline for the CFD Simulation of Flows in the Urban Environment, COST Action 732: Quality Assurance and Improvement of Microscale Meteorological Models, 2007.
[63] S. Kenjereš, S. de Wildt, T. Busking, Capturing transient effects in turbulent flows over complex urban areas with passive pollutants, Int. J. Heat Fluid Flow 51 (2015) 120–137.
[64] T. Van Hooff, B. Blocken, Coupled urban wind flow and indoor natural ventilation modelling on a high-resolution grid: a case study for the Amsterdam ArenA stadium, Environ. Model. Software 25 (1) (2010) 51–65.
[65] F. Baetke, H. Werner, H. Wengle, Numerical simulation of turbulent flow over surface mounted obstacles with sharp edges and corners, J. Wind Eng. Ind. Aerod. 35 (1990) 129–147.
[66] G. Oh, K.M. Noh, H. Park, J.I. Choi, Extended synthetic eddy method to generate inflow data for turbulent thermal boundary layer, Int. J. Heat Mass Tran. 134 (2019) 1261–1267.
[67] C. Peitzmeier, C. Loschke, H. Wiedenhaus, O. Klemm, Real-world vehicle emissions as measured by in situ analysis of exhaust plumes, Environ. Sci. Pollut. Res. 24 (29) (2017) 23279–23289.